International Journal of Multiphase Flow 36 (2010) 570–587

Contents lists available at ScienceDirect

International Journal of Multiphase Flow

journal homepage: www.elsevier.com/locate/ijmulflow

Time and spatially resolved measurements of interfacial waves in vertical annular flow

R.J. Belt [a,*], J.M.C. Van't Westende [a], H.M. Prasser [b], L.M. Portela [a]

[a] Multi-Scale Physics Department, Delft University of Technology, J.M. Burgerscentrum for Fluid Mechanics, Prins Bernhardlaan 6, 2628 BW Delft, The Netherlands
[b] ETH Zürich, Department of Mechanical and Process Engineering, ML K 13, Sonneggstrasse 3, 8092 Zürich, Switzerland

ARTICLE INFO

Article history:
Received 24 September 2008
Received in revised form 24 February 2010
Accepted 10 March 2010
Available online 15 March 2010

Keywords:
Vertical annular flow
Interface reconstruction
Film thickness
Interfacial structures
Disturbance waves

ABSTRACT

Film thickness measurements have been performed in a vertical air/water annular flow in a pipe of 0.05 m diameter. A sensor has been built which allows to measure the film thickness evolution in time at 320 positions, such that the interface of the vertical annular flow can be reconstructed. The large-scale structures moving on the interface are described statistically, with a special attention to the disturbance waves. Probability density functions and mean statistics are given for the height, length, velocity, frequency and spatial distribution of the disturbance waves. In particular, it is shown that the disturbance waves are three-dimensional structures with large height fluctuations in the circumferential and axial direction, giving a meandering path between the maximum height around the circumference. It is also shown that the disturbance waves can flow with a slight inclination with respect to the axial direction. Finally, the disturbance waves are shown to be located randomly in space, within a Gamma distribution whose order only depends on the liquid superficial velocity. Due to the nature of the Gamma distribution, it could indicate that the spatial distribution of the disturbance waves results from a cascade of coalescence processes between the original disturbance waves on the film.

1. Introduction

Annular flow is a two-phase flow configuration which can occur in pipes used for the production and transport of natural gas. In annular flow, the liquid (e.g. gas condensates or oil) flows partly as a thin and wavy film along the wall, and partly as droplets entrained in the turbulent gas core. For improvement of the natural gas production processes, it is required to predict accurately the phase distribution in the pipe. In vertical annular flow, the distribution is governed by the continuity and momentum balances in the axial direction. From the quantities involved in the axial momentum balance on the film, the interfacial shear-stress and the gravitational force on the film clearly play a major role in the prediction. The gravitational force depends directly on the mean film thickness, which, in turn, is related to the interfacial shear-stress and the amount of droplets entrained in the gas core. Therefore, a key point in the prediction of the phase distribution in vertical annular flow is the interfacial shear-stress and the entrainment.

The interfacial shear-stress and the entrainment result from the interaction between the gas flow and the liquid film at the interface, therefore they must be closely related to the structures moving on the interface. Several types of interfacial structures can be observed in annular flow, of which the "disturbance" waves are the most prominent ones (also referred to as "roll" waves in the literature). These surges have a height of about four times the mean film thickness, are coherent in the streamwise direction, and move with an approximately constant wave velocity (Azzopardi, 1997; Wallis, 1969). In pipes of diameter smaller than roughly 0.1 m, the disturbance waves cover the entire circumference of the pipe (Azzopardi, 1997), and their length is typically of the order of the pipe diameter. Although the length of the disturbance waves is much larger than their height, they are quite different from hilly two-dimensional structures, over which the turbulent gas core could be in a quasi steady-state. Instead, as can be seen from pictures in Hewitt et al. (1990) or Badie et al. (2001), the disturbance waves show large height variations, such that the disturbance waves are truly three-dimensional structures. Next to the coherent disturbance waves, other non-coherent structures exist. For instance, a large number of irregularities of small amplitude cover the interface, which are not coherent over large distances. In the literature, these structures are referred to as "ripple" waves, and are believed to be surface tension waves (Asali and Hanratty, 1993). Also non-coherent structures of large amplitude, similar to that of the disturbance waves, can occur on the interface. For instance, Sekogushi and Takeishi (1989) and Wolf et al. (1996) have recognized the occurrence of "ephemeral" waves, which look similar to disturbance waves. However, they are less frequent, and

* Corresponding author at: Total E&P, Process Department, 2 Place Jean Millier, La Défense 6, 92400 Courbevoie, France. Tel.: +33 147442735.
E-mail address: roel.belt@total.com (R.J. Belt).

0301-9322/$ - see front matter © 2010 Elsevier Ltd. All rights reserved.
doi:10.1016/j.ijmultiphaseflow.2010.03.004

have a velocity which is different from that of the disturbance waves, with larger fluctuations. Therefore, these waves will merge with the disturbance waves, and have a short lifetime.

The interfacial structures promote an extra drag on the gas flow due to the pressure forces acting on them, similar to roughness. Due to the large amplitude and the three-dimensional character of the disturbance waves, it is likely that the disturbance waves have the largest contribution to the extra drag. In Belt et al. (2009), it is shown that the interfacial friction can be predicted accurately using the existing theory on roughness in single-phase turbulent pipe flows. The sand-grain roughness, which is needed in this formulation, is shown to be related to the frontal area of the disturbance waves seen by the gas flow. However, this frontal area involves the height, frequency and velocity of the disturbance waves, for which the behavior is not well known. On the other hand, Hanratty (1991) suggests that the interfacial friction is mainly due to ripple waves on the film, which act like sand roughness. Although it can be questioned whether the impact of ripples on the extra drag can be that large to give the observed friction in annular flow (the height of the ripples being not larger than roughly 30 wall-units, therefore not exceeding the buffer layer in the turbulent gas flow), the structure of the ripples is also of interest.

The amount of entrainment results from a balance between the entrainment and deposition rate of droplets from and onto the film (Pan and Hanratty, 2002). Especially for the entrainment rate, a physically-based prediction is lacking. It is known that the entrainment of droplets from the film occurs by removal of the small waves riding on the disturbance waves (Azzopardi, 1997; Woodmansee and Hanratty, 1969). Therefore, to get more insight into the entrainment rate, a detailed representation of the disturbance waves is needed. For instance, it could be suggested that the amount of entrained droplets depends on the length and frequency of the disturbance waves. For the ballistic deposition of large droplets (James et al., 1987; Lopes and Dukler, 1986), information must be known on (i) the velocity of the droplets entrained from the disturbance wave, which could be approximated by the disturbance wave velocity, and on (ii) the angle of the trajectory, which could be related to the three-dimensional structure of the disturbance waves.

From the discussion above, it is clear that a detailed representation of the interfacial structures, especially of the disturbance waves, is needed to improve the understanding and modeling of both the interfacial friction and entrainment of droplets from the film. Therefore, in this work, we focus on the waviness of the interface, using experiments. Especially, we will pay attention to the characterization of the disturbance waves. To that purpose, we developed a non-intrusive film thickness probe able to reconstruct the interface in time and space, and to give a quantitative description of the interfacial structures, which was not possible until now.

First, the measurement technique will be explained, together with the experimental set-up. Then, a qualitative picture of the interfacial waves measured in the study will be presented. Next, we will present the approach used to extract the disturbance waves from the signals. Finally, we will present the results on (i) the mean film thickness and the mean wave velocity, (ii) global statistics on the interfacial structure, and (iii) the statistics of the disturbance waves, such as their height, length, frequency, circumferential behavior and spatial distribution.

2. Experimental set-up and the film thickness measurement technique

2.1. Experimental set-up

The experimental set-up of the air/water annular flow consists of a vertical, cylindrical pipe, made of perspex, of inner diameter $D = 0.05$ m and of total length $L = 12$ m (see Fig. 1). Dry air is injected with a compressor at the bottom of the pipe. Tap water is fed into the pipe through a porous wall 1 m downstream of the gas inlet, in order to avoid eventual gas entrance effects on the liquid film at its entrance in the pipe. The mass-flow rates of air and water entering the pipe are measured with rotameters. The film thickness sensor is placed about 6.5 m ($=130 \cdot D$) downstream the water inlet. The liquid film is removed from the pipe through an annulus about 2.5 m ($=50 \cdot D$) downstream the film thickness sensor, therefore avoiding any exit effects on the film thickness measurements. In the water coming from the annulus, temperature and conductivity of the water are measured. The water conductivity is required to obtain the film thickness from the raw data of our film thickness sensor. After the film withdrawal section, the droplet-laden gas core flows through 2 m of pipe ($=40 \cdot D$), after which the water is separated from the air and then collected. Finally, the pressure-gradient in the vertical annular flow is measured between 4 m ($=80 \cdot D$) and 7 m ($=140 \cdot D$) downstream of the water inlet using a differential manometer (Van't Westende et al., 2007).

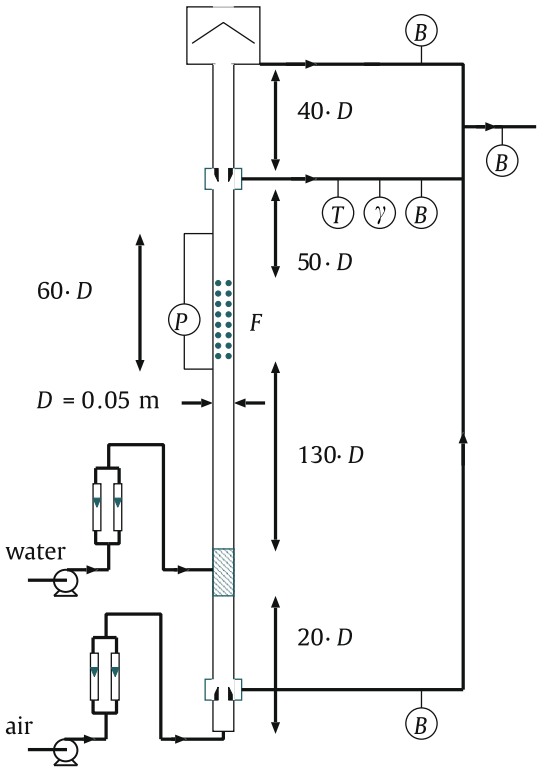

Fig. 1. Experimental set-up. At T, γ and P, the temperature, the conductivity and the pressure-gradient are measured, respectively. The film thickness probe is located at F. At B, the mass-flow rate of water can be measured with a balance.

The results presented in this work correspond to the annular flow regime without flow reversal, i.e. above or at the minimum of the pressure-gradient vs. gas flow-rate curve (Zabaras et al., 1986). Therefore, the gas superficial velocity U_{GS} in the measurements is equal to or larger than 22 m/s (see Table 1). The liquid superficial U_{LS} is such that the interface is covered by disturbance waves, except at the lowest one, at which the Reynolds number Re_{LS} (based on the liquid superficial velocity and the pipe diameter) is equal to 238. Indeed, this Reynolds number is smaller than the critical one, Re_{LS}^{crit}, which is equal to roughly 250–350 in a pipe of 0.05 m diameter (Azzopardi, 1997), below which disturbance waves do not occur. However, as we will show in Sections 3 and 5, it does not necessary mean that large height fluctuations do

Table 1
Liquid and gas superficial velocities, U_{LS} and U_{GS} respectively, for the measurements presented here. Re_{LS} and Re_{GS} are the Reynolds numbers based on the pipe diameter and the liquid and gas superficial velocity, respectively. We note that the values of the gas superficial velocities can vary 0.3 m/s maximum around the values in the tables at the different U_{LS}.

U_{LS} (m/s)	5.3×10^{-3}	9.6×10^{-3}	1.9×10^{-2}	4.0×10^{-2}	8.2×10^{-2}
Re_{LS}	238	431	855	1805	3705
U_{GS} (m/s)	21.9	26.2	31.0	36.4	42.1
Re_{GS}	75×10^3	89×10^3	106×10^3	124×10^3	143×10^3

not exist in this regime. The liquid superficial velocities in the experiments are also shown in Table 1.

2.2. Film thickness measurement technique

The film thickness is measured using a conductivity-based technique. For a conducting liquid (e.g. water), the liquid film is electrically conducting with a conductance proportional to the film thickness, whereas the droplet-laden gas core is not. Therefore, the idea of the measurement technique is to impose an electrical potential between a pair of electrodes in contact with the liquid film and measure the resulting current, which is a function of the conductance of the liquid film, hence of its thickness. Such a technique has been used extensively in the literature (e.g. Coney, 1973; Brown et al., 1978; Zabaras et al., 1986; Jayanti et al., 1990; Paras and Karabelas, 1991; Fore and Dukler, 1995). The main difference of the present technique with others in the literature is that, in the literature, the time signal of the film thickness is measured at only a few positions in the annular flow, whereas we are measuring the film thickness evolution in time at many positions (in our case: 320 positions), giving us a spatial reconstruction of the film in the annular flow, and, therefore, spatial information on the interface. The concept, the calibration and the validation of the measurement technique are described in detail in Belt (2007). Since conductivity-based film thickness measurement techniques have been used extensively in the literature, below we only give a short introduction to our technique.

The film thickness sensor is shown in picture 2 and it is represented schematically in Fig. 3. The sensor is a repetition in the axial direction of the unit n (see Fig. 3), which consists of one "transmitter" ring electrode T_n, 32 "receiver" island electrodes R_n equally spaced around the circumference, and one insulation ring I. The ring and island electrodes are flush with the inner pipe wall, making our film thickness sensor non-intrusive. Since we have a repetition of 10 units in the axial direction, we obtain a measuring matrix of 32 measurement locations in the circumferential direction times 10 measurement locations in the axial direction. During the signal acquisition, the transmitter electrodes are activated successively by supplying them with a rectangular voltage pulse. For each transmitter activation, the resulting current is measured successively at the receiver electrodes in the corresponding unit. A full cycle necessary to activate all transmitters and to measure the current at all receivers takes 0.2 ms, therefore the total measuring rate is 5 kHz, i.e. much higher than the physical phenomena observed in annular flow. The principle and the signal acquisition hardware are the same as those in the electrode-mesh sensor of Prasser et al., 1998, 2002 and details can be found therein.

Fig. 2. Picture of the film thickness sensor. The conductance is measured between a ring-electrode and island-electrode flush with the wall.

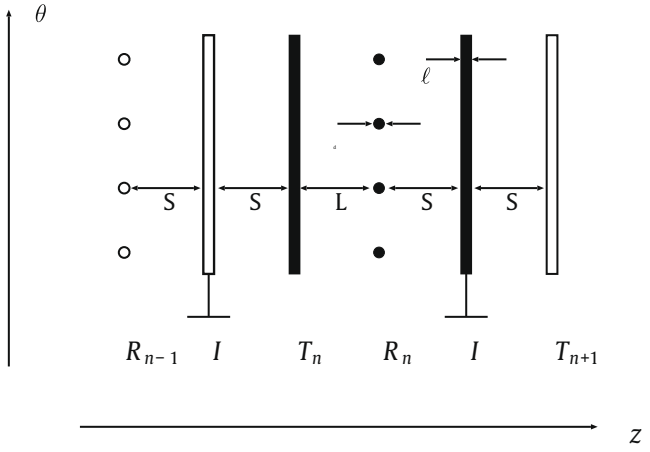

Fig. 3. Partial schematic representation of the nth unit of the sensor. The nth unit, in black, consists of one transmitter ring electrode T_n, 32 receiver island electrodes (only 4 of the 32 receivers are represented in the figure), and one grounded insulation ring I. The cylindrical sensor is opened in the representation. The z-axis represents the axial direction (the flow direction), and the θ-axis the circumferential direction. The distance L is equal to 6 mm, the distance S to 3 mm, and the distance ℓ to 2 mm. Only the receivers R_{n-1} and the insulation ring I of the previous unit $n-1$, and the transmitter T_{n+1} of the next unit $n+1$ are shown in the figure.

In our film thickness measurements, it is important to avoid interference between the 320 measurement locations, which explains the necessity, among others, of the insulation rings I in Fig. 3. During the signal acquisition, a transmitter ring is activated and the current is sampled at a receiver island in the same unit. However, the major part of the current flows from the activated transmitter to the neighboring receivers of the one which is sampled, and to the transmitters and receivers of other units. This issue is even more important, since, in practice, our receiver islands from the 10 units at the same circumferential position are connected (in order to have only 32 signal acquisition circuits instead of 320). So, measures must be taken in order to reduce the loss of spatial resolution in the film thickness measurement due to the currents flowing from the activated transmitter electrode to the receivers electrodes of the neighboring units, or "cross-talk". Second, it must be avoided that transmitter electrodes from other non-activated units depart from zero potential due to this kind of parasitic currents. Without appropriate countermeasures, this would also lead to cross-talk and a loss of spatial resolution. The parasitic currents cannot be avoided, however, their effect on the measurement can be suppressed by designing the output and input circuits with an impedance significantly lower than the impedance of the fluid, which guarantees a zero potential at the transmitter and receiver electrodes, except at the activated transmitter. Furthermore, the insulation rings I with zero potential are placed between each unit in order to reduce the current flowing from one unit to the other,

and therefore to uncouple the units. In this way, we only measure the current flowing in the "control-volume" between the activated transmitter and the selected receiver from the same unit.

In Belt (2007), the amplitude of cross-talk is assessed numerically. The potential field equation is solved for a liquid film of constant thickness above the sensor. Hence, the numerical set-up is the same as in the experimental calibration presented below. First, we note that a calibration curve is obtained from these simulations by using different heights for the liquid film, and that it is in very good agreement with the experimental calibration curve. Next, the simulations allow to compare the current arriving at the closest receiver (in the unit of the activated transmitter), and the current arriving at the second closest receiver at the same circumferential position (in the unit adjacent to that containing the activated transmitter). Since in practice those receivers are connected, the comparison between those two currents gives an idea of the loss of resolution in the axial direction. The simulations show that the cross-talk (the signal at the second closest receiver) is negligible for a film thickness up to 2 mm. For a film thickness between 2 and 4 mm, the cross-talk increases to about 10% of the signal, which is still acceptable.

The sensor is calibrated experimentally using a static liquid film. It is made by inserting a non-conducting insert of known diameter into the sensor, mimicking the gas core, and by filling the volume left between sensor and insert with water. A calibration curve is determined for each receiver with the fit-model $A \cdot (1 - \exp(-B \cdot \delta))$, where δ is the gap thickness, and A and B the fitted parameters. One typical example of a curve fit is shown in Fig. 4. It shows that the sensitivity of the sensor decreases for increasing film thickness, and that a film thickness up to about 3.5×10^{-3} m can be measured with sufficient sensitivity. In the results section (Figs. 27 and 28), we show the probability density functions of the height of the disturbance waves, which are the largest structures in annular flow. In these figures, we can see that the probability of having a disturbance wave larger than 3.5×10^{-3} m is small, therefore, the height of most of the interfacial structures is measured with a good resolution. Furthermore, we note that saturation of the current occurred only rarely.

In the measurements, the water conductivity can vary due to temperature changes or eventual water contaminants. Therefore, it is likely that the measurements are performed with water at a different conductivity than that in the calibrations. Since the conductance is proportional to the water conductivity, a correction must be applied to the calibration curves, based on the actual conductivity during the measurements in annular flow. The correction is obtained by:

$$A_{\text{meas}} = \frac{\gamma_{\text{meas}}}{\gamma_{\text{cal}}} A_{\text{cal}} \quad (1)$$

$$B_{\text{meas}} = B_{\text{cal}} \quad (2)$$

where γ is the water conductivity, and where the subscripts "meas" and "cal" refer to the measurements and calibrations, respectively. It is checked experimentally in Belt (2007), by doing calibrations at different conductivities, that indeed the parameter A is a linear function of the conductivity γ, and that the parameter B represents the inverse of a characteristic length of the sensor, which is constant.

A vertical annular flow is axisymmetric, hence, the mean film thickness should be constant around the circumference. The comparison of the 32 mean film thicknesses measured around the circumference gives a value for the accuracy of the film thickness measured in annular flow with our measurement technique. The accuracy (twice the standard deviation) is about 12% of the film thickness.

The current measured at a receiver is a function of the film conductance integrated over the control-volume in between the transmitter and receiver. Therefore, at each measurement location, we measure at each instant a mean film thickness averaged over this control-volume. This issue is intrinsic to the conductivity-based film thickness measurement technique, and is also true for the conductivity-based measurements in the literature. In our sensor, the control-volume is delimited in the axial direction by the transmitter and receiver electrodes, and in the circumferential direction by the neighboring measurement locations. Hence, the control-volume has roughly a length of 6×10^{-3} m (the axial distance between the transmitter and receiver) and a width of 4.9×10^{-3} m (the distance in the circumferential direction between two neighboring receivers). Interfacial structures with a size smaller than roughly these distances cannot be measured accurately with the measurement technique. For instance, the axial distance of 6×10^{-3} m is slightly larger than the wavelength of the ripple waves (Asali and Hanratty, 1993), and therefore it is expected that ripple waves are not measured correctly. However, in our experiments, the length of the disturbance waves is roughly equal to 0.05 m (see the results section), i.e. one order of magnitude larger than the axial distance between the transmitter and receiver. Therefore, a "local" height of the disturbance waves can be measured with the sensor. We note that in Belt (2007), measurement results are presented with this sensor and with a sensor having an axial distance of 3×10^{-3} m between the transmitter and receiver, i.e. a smaller control-volume. The measured mean film thickness in vertical annular flow is almost identical for the two sensors. This means that the height of the large interfacial structures, which have the largest contribution to the mean film thickness, is correctly measured.

The measurement locations are separated by 4.9×10^{-3} m in the circumferential direction and 19.5×10^{-3} m in the axial direction. This corresponds to the spatial resolution of the sensor, which is rather low (see also next section, in which snapshots are shown). Indeed, to observe an interfacial structure in a snapshot of the interface (i.e. the visualization of all measured film thicknesses at one instant), at least a few points are required inside the structure. Hence, structures having a size smaller than roughly the spatial resolution cannot be observed in the snapshots. The spatial resolution is particularly restrictive in the axial direction, since only the

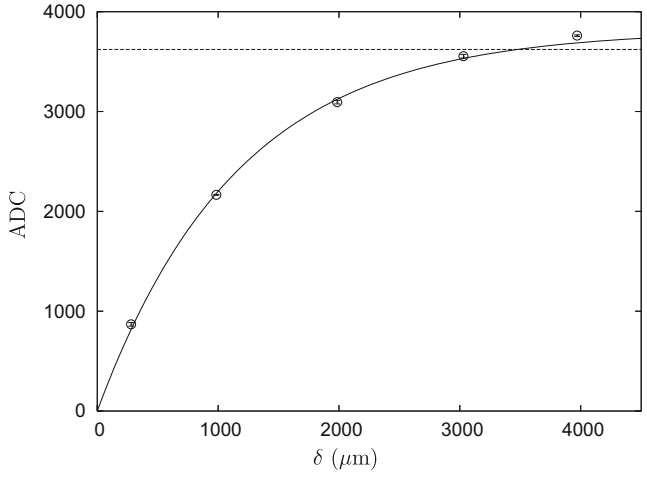

Fig. 4. Typical example for a calibration curve giving the relation between the film thickness (in μm) and the current of the receiver (in ADC units). The open dots correspond to the calibration points, the corresponding error bars to twice the standard deviation. The solid line correspond to the fit used for the calibration. The dashed line corresponds to 95% of the maximum value of the fit. Assuming an error in the calibration less than 5%, the signal (i.e. the corresponding film thickness) below the dashed line can be measured accurately.

large disturbance waves have a length larger than the axial distance between two measurement locations. However, because of the high temporal resolution (5000 Hz), structures with an axial length smaller than 19.5×10^{-3} m can be seen by using the time-signals. Indeed, the interfacial structures mainly flow in the axial direction. Furthermore, during their lifetime, the structures flow as one entity, with a defined velocity for this entity. Therefore, the shape of the interfacial structures in space can be obtained from the height variations in time at one position, if each interfacial structure is assumed to be "frozen" during its crossing over the measurement location. This approach is usual in the field of single-phase turbulent flows. Note that the small-scale variations on each structure should be regarded with caution, since they may have a different velocity and lifetime than the large-scale entity. Then, the comparison of the time-signals at the 320 measurement locations can give statistical information on the coherence and the velocity of the interfacial structures. This approach is used in the article in order to obtain the statistical information on the disturbance waves (see Section 5).

3. Waves in vertical annular flow

The different types of waves in annular flow were briefly described in the introduction. This section is used to illustrate qualitatively some of their properties which were raised in the introduction, with typical snapshots of the interface and time-signals, and to provide general qualitative conclusions on the interfacial structure. Due to the limited spatial resolution (see previous section), the snapshots should be interpreted with care, and can only provide qualitative information. A quantitative description of the interfacial waves, based on the time-signals at the 320 measurement locations, can be found in the results section (see Section 5).

3.1. Disturbance waves

Two snapshots of the interface are shown in Fig. 5. The snapshots show two consecutive disturbance waves, with in between small non-coherent fluctuations. It is clear from Fig. 5 that the disturbance waves are the prominent interfacial structures. Furthermore, Fig. 5 shows that each disturbance wave has large height fluctuations in the circumferential direction. Hence, the disturbance waves are quite different from hilly two-dimensional structures, and show instead a clear three-dimensional character. The height of the disturbance wave has also changed in the two consecutive snapshots for a given circumferential position. This means that the height of the disturbance wave evolves in time, and/or that it varies in the axial direction. It cannot be concluded from the snapshots which of the two explanations is the correct one, since (i) we do not have sufficient spatial resolution, and (ii) a different part of the disturbance wave is measured in the two snapshots, as the wave has traveled.

The three-dimensionality of the disturbance waves, and their variation in both the circumferential and axial directions, is even more clear in Fig. 6, which shows the height of a disturbance wave passing by at one given axial location as a function of the circumferential position. We note that the height variations in the circumferential direction do not correspond to measurement errors, since they have an amplitude much larger than the experimental error and exist longer than one sampling period. One could argue that these variations are due to eventual bubbles entrapped in the disturbance waves. However, we do not expect the disturbance waves to have bubbles large enough to explain these large variations. Furthermore, large variations of the disturbance wave height in the circumferential direction are also observed in the pictures made by Badie et al. (2001).

The structure of the disturbance waves can be reconstructed from the time-signals, using the assumption that the disturbance wave is frozen during its crossing over the measurement location. This assumption is expected to be valid for at least the large-scale fluctuations of the disturbance wave. Different time-signals around the circumference are shown in Fig. 7. Fluctuations of large amplitude are often measured at roughly the same time around the circumference. Those height fluctuations which are coherent over the circumference correspond to the disturbance waves. Note that it is clear from the snapshots in Figs. 5 and 6 that the height of the disturbance waves varies significantly in the circumferential direction. Therefore, in Fig. 7, one of the time-signals can be at a circumferential position such that the hollow of the disturbance wave height fluctuations is shown. In that case, the disturbance wave might not be as apparent as in the other time-signals, although the disturbance waves cover the entire circumference. In Fig. 8, we show the time-signals of Fig. 7 but over half of the circumference, such that the figure can be enlarged and the small-scale structure of the interface can be magnified. From Figs. 7 and 8, it can be seen that: (i) the height of the disturbance waves varies in the circumferential and axial direction, (ii) the disturbance waves are coherent over the entire circumference, (iii) the disturbance waves can flow with a slight inclination with respect to the axial direction, since they do not arrive exactly at the same time in the time-signals around the circumference (this point is discussed further below), and (iv) the length of the disturbance waves is not constant. The non-constant length of the disturbance waves could be partially explained by the coalescence of the disturbance waves with the small-scale fluctuations in between the disturbance waves, which have also a non-negligible length (in the order of 10^{-2} m). Indeed, in between the disturbance waves, the film is covered by small-scale fluctuations (see Fig. 8). Those small-scale fluctuations are not coherent over the circumference, since they cannot be found in all time-signals around the circumference. Note that, in some cases, their amplitude can be quite

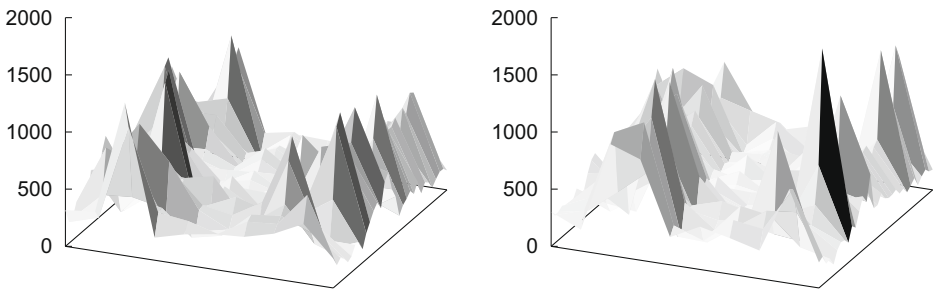

Fig. 5. Raw instantaneous film thickness data (in μm) at two distinct instants t at the 320 measurement locations. The film flow is in the axial direction from the left to the right, over a distance of 0.176 m. The snapshots are separated by 0.002 s. The pipe is opened up for visualization purposes, i.e. the front and the back of the plots are in reality in contact. The snapshots correspond to a vertical annular flow at $U_{LS} = 0.08$ m/s and $U_{GS} = 42$ m/s.

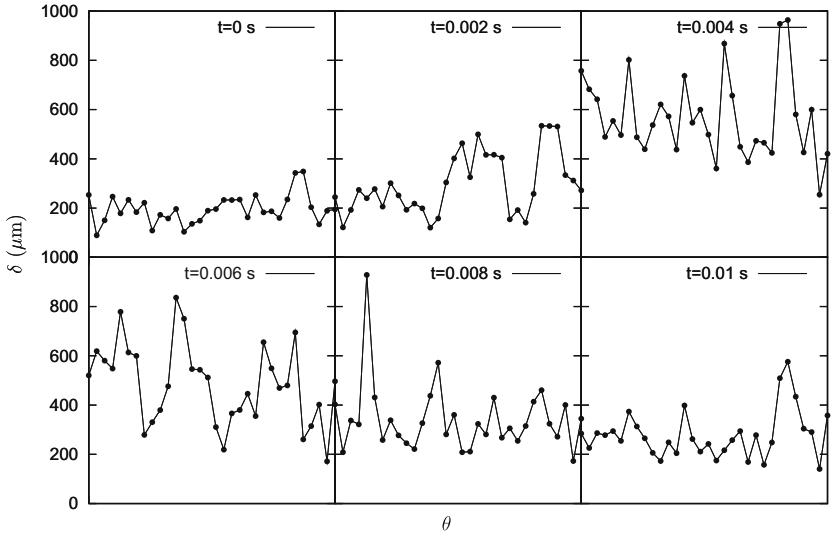

Fig. 6. Progress in time of the height of a disturbance wave at one axial location (the x-axis corresponds to the circumferential position). The figures are separated by 0.002 s, the picture at $t = 0$ s corresponds to the start of a disturbance wave, $t = 0.01$ s to the end of that disturbance wave. The liquid and gas superficial velocities are equal to $U_{LS} = 0.02$ m/s and $U_{GS} = 42$ m/s, respectively.

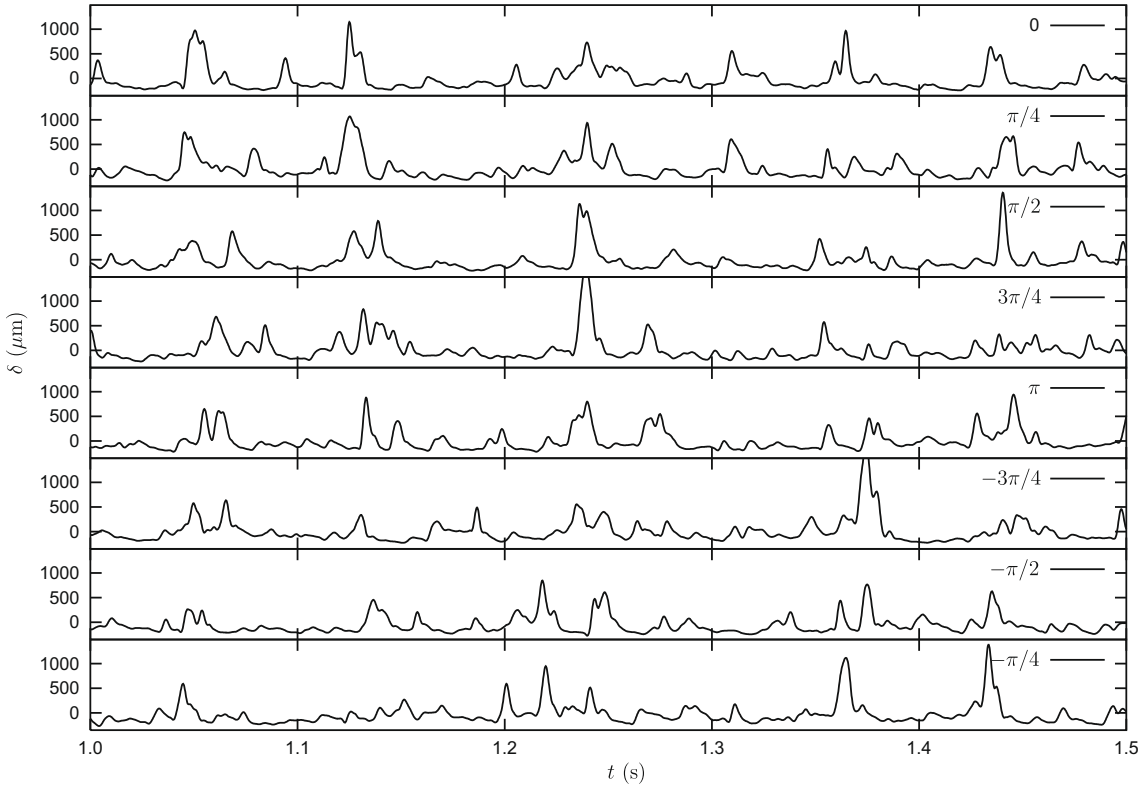

Fig. 7. Time-signals of the film height at different circumferential positions for one given axial position. The mean film thickness has been subtracted from the time-signals, i.e. the time-signals shown in the figure have a zero mean. The liquid and gas superficial velocities are equal to $U_{LS} = 0.08$ m/s and $U_{GS} = 42$ m/s, respectively. The velocity of the disturbance waves is equal to 2.6 m/s and the mean film height is equal to 329 μm (see Section 5).

large, similar to that of the disturbance waves. Those non-coherent fluctuations are discussed in Section 3.2.

The second disturbance wave in Fig. 8 is magnified in Fig. 9. The zoom shows again that the disturbance waves are not two-dimensional smooth hilly structures. We note that the smallest fluctuations on the disturbance waves which can be measured in Fig. 9 have a duration of roughly 0.002 s. Indeed, the measured film thickness is averaged over the control-volume in between the electrodes which has a length of 0.006 m, and the disturbance waves move in this case with a velocity equal to 2.6 m/s. In reality, the disturbance waves are probably covered by smaller fluctuations, however they are not visible in Fig. 9. In the results section, we show that the pdf of the length of the disturbance waves is broadly distributed, and that the average length is roughly equal to the pipe diameter for all flow conditions. In Fig. 9, a length equal to the pipe diameter corresponds to roughly 0.01 s. Indeed, in Fig. 9,

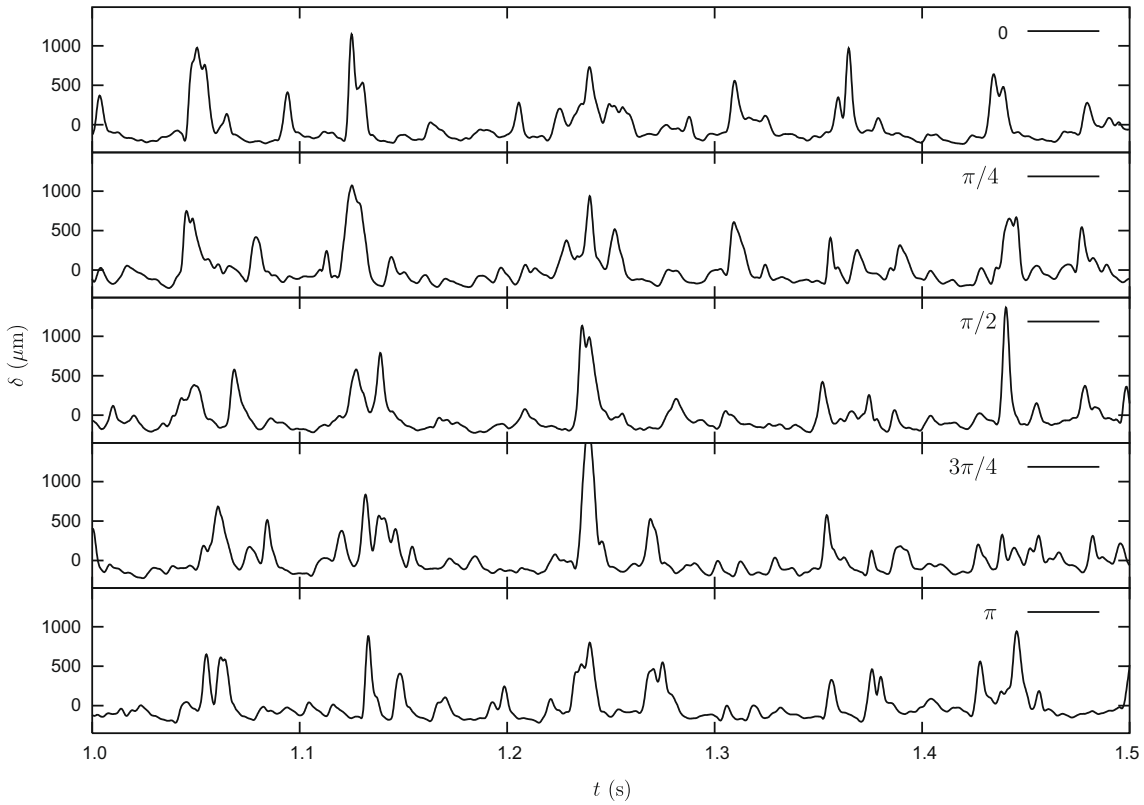

Fig. 8. Time-signals of the film height at different circumferential positions for one given axial position. The mean film thickness has been subtracted from the time-signals, i.e. the time-signals shown in the figure have a zero mean. The liquid and gas superficial velocities are equal to U_{LS} = 0.08 m/s and U_{GS} = 42 m/s, respectively. The velocity of the disturbance waves is equal to 2.6 m/s and the mean film height is equal to 329 μm (see Section 5).

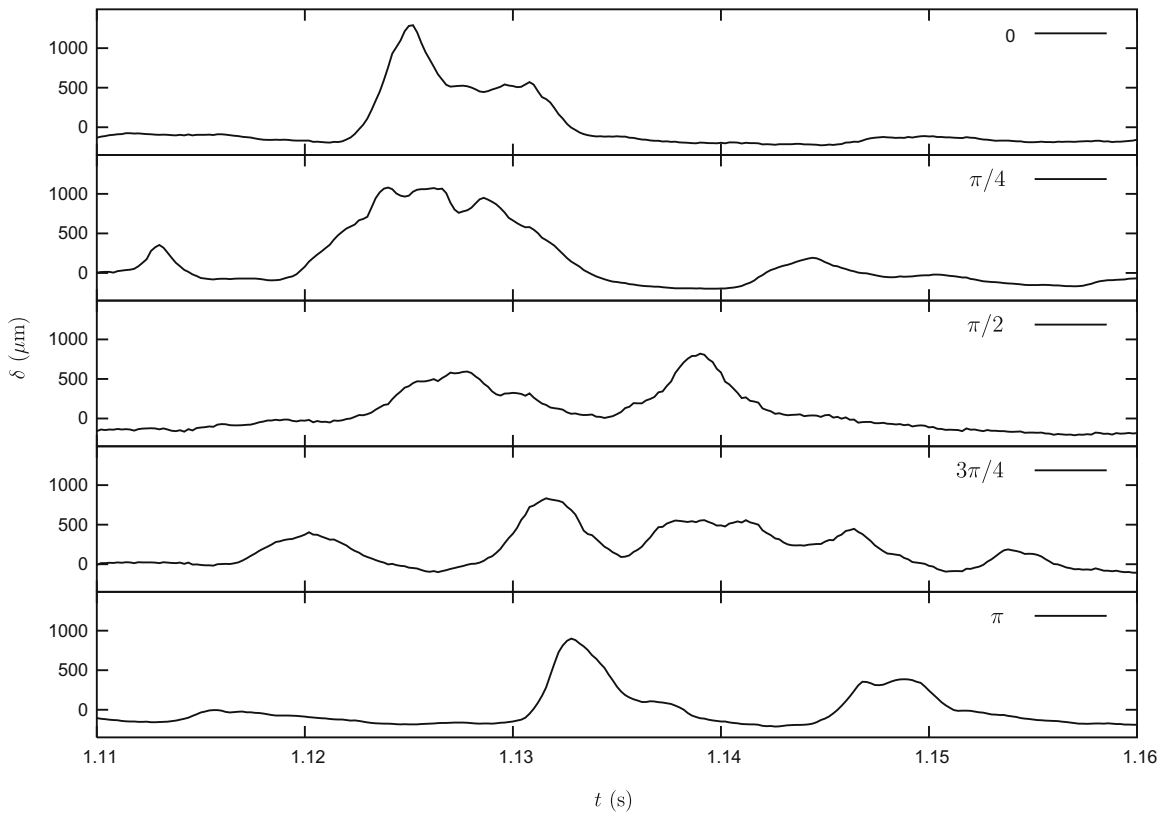

Fig. 9. Zoom on a disturbance wave in the time-signals of the film height at different circumferential positions for one given axial position. The mean film thickness has been subtracted from the time-signals. The liquid and gas superficial velocities are equal to U_{LS} = 0.08 m/s and U_{GS} = 42 m/s, respectively. The velocity of the disturbance waves is equal to 2.6 m/s and the mean film height is equal to 329 μm (see Section 5).

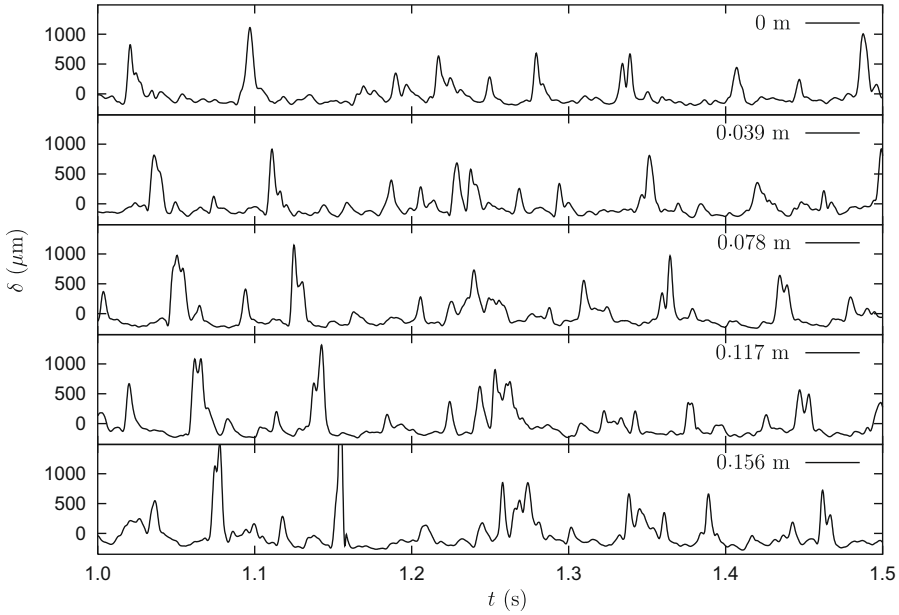

Fig. 10. Time-signal of the film thickness at different axial positions for one given circumferential position. The mean film thickness has been subtracted from the time-signals. The liquid and gas superficial velocities are equal to U_{LS} = 0.08 m/s and U_{GS} = 42 m/s, respectively. The velocity of the disturbance waves is equal to 2.6 m/s and the mean film height is equal to 329 μm (see Section 5).

the length of the disturbance wave is of this order, but it varies in the circumferential direction. The height of the disturbance wave also varies significantly over its length. A further interesting observation in Fig. 9 is that the peaks of the disturbance wave are not measured exactly at the same time. This means that the disturbance waves are not aligned perpendicularly to the flow direction, but that they can flow with a slight inclination with respect to the axial direction. This point is discussed in the results section.

Fig. 10 shows the time-signals measured at different axial positions, for one given circumferential position. It can be seen that the disturbance waves are coherent, and that the small-scale fluctuations in between the disturbance waves are not. All disturbance waves seem to flow with a constant velocity. Moreover, the time-signals show that the structure and height of the disturbance waves evolve in time.

3.2. Non-coherent small-scale film height fluctuations

In the measurement technique, the instantaneous film thickness obtained at each measurement location corresponds to an instantaneous film thickness averaged over the control-volume between the transmitter and receiver electrodes. Therefore, interfacial structures with a size smaller than that of the control-volume are averaged in the value of the instantaneous film thickness. In particular, the axial length of the control-volume (0.006 m) is larger than the wavelength of the ripple waves (equal to a few millimeters, according to Asali and Hanratty, 1993), meaning that ripple waves cannot be resolved in our measurements. However, in between the disturbance waves in Figs. 5, 8 and 10, non-coherent fluctuations can be observed. The height of these fluctuations is generally smaller than the disturbance waves, but is larger than the ripple waves, typically equal to 10–20 μm (Asali and Hanratty, 1993). First, we can see in Figs. 8 and 10 that the length of these non-coherent height fluctuations is in the order of 10^{-2} m. This is larger than the capillary length $(\sigma/(\rho_L g))^{1/2}$, equal to 2.7×10^{-3} m for our experimental conditions (σ is the surface tension, ρ_L the density of the liquid and g the gravitational acceleration). Therefore,

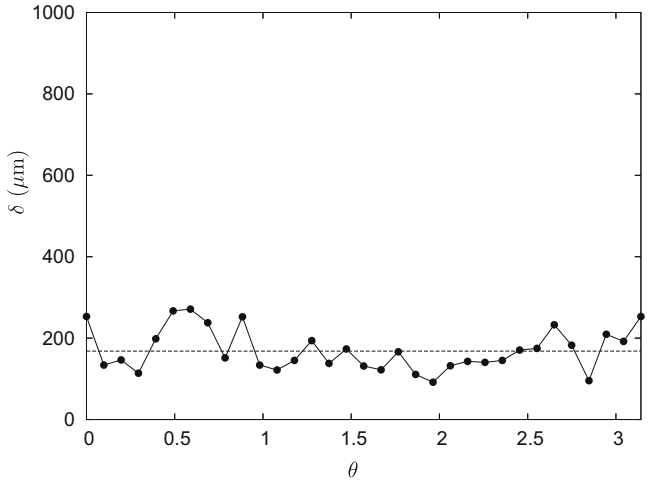

Fig. 11. Non-coherent film height fluctuations in the circumferential direction, at one given axial position. The dashed line corresponds to the mean value of the film height in the figure. The liquid and gas superficial velocities are equal to U_{LS} = 0.02 m/s and U_{GS} = 42 m/s, respectively.

these structures are probably not dominated by surface tension forces as it is the case for ripple waves. Note that, in the results section, we show that the energy in the power spectrum corresponding to these non-coherent height fluctuations decreases with a power −4, i.e. the same power as for wind-generated gravity waves on oceans (Phillips, 1985). Second, Figs. 8 and 10 show that these height fluctuations are not coherent in the axial and circumferential direction. An example of the film thickness around the circumference in between two consecutive disturbance waves (see Fig. 11) shows that the non-coherent height fluctuations have a three-dimensional character.

Some non-coherent height fluctuations in the time-signals have a large amplitude similar to that of the disturbance waves. For example, the second peak in Fig. 8 (with the angle equal to 0) and in Fig. 10 (with an axial distance of 0.078 m) has a large

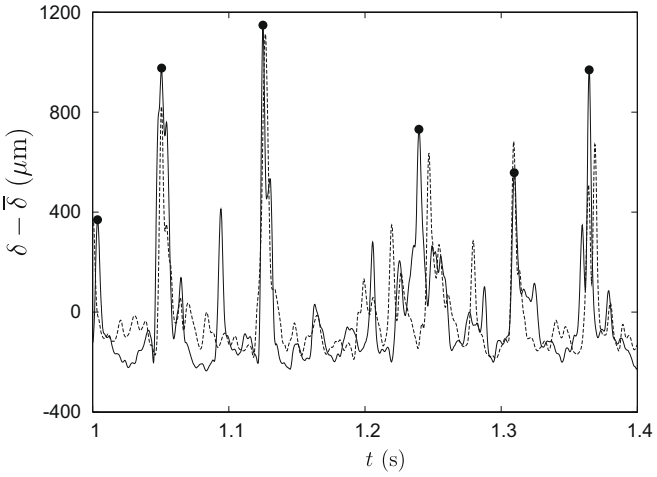

Fig. 12. Typical example of two time-signals of the film thickness. The solid line corresponds to the time-signal at a reference location, the dashed line to the time-signal at a different axial location, and shifted in time with the spacing between the two points over the velocity of the disturbance waves. The dots correspond to events which are qualified as disturbance waves. In between the disturbance waves, we can see many non-coherent height fluctuations. These can be quite large sometimes, e.g. here at $t \approx 1.1$ s. The latter are referred to as "ephemeral" waves in the literature.

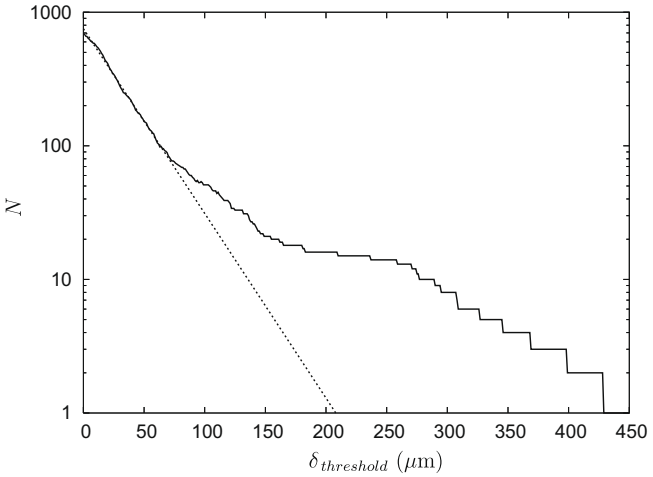

Fig. 13. Typical behavior of the amount of events N above the threshold $\delta_{threshold}$ (solid line), with its exponential fit (dashed line) in the region where the decay of the amount of waves N is a Poisson distribution of the threshold $\delta_{threshold}$. Note that the origin of the threshold corresponds to the mean film thickness. In the case presented in the figure, the threshold is set equal to 50% · 73 μm above the mean film thickness, where the 50% corresponds to an arbitrary safety margin to ensure that all disturbance waves are listed.

amplitude, but it is not coherent in the axial and circumferential direction, as it can be seen from the other time-signals in Figs. 8 and 10. Those non-coherent height fluctuations of large amplitude were referred to as "ephemeral" waves by Wolf et al. (1996). However, it is not clear what distinguishes them from the smaller non-coherent height fluctuations (referred to as ripples by Wolf et al. (1996), wrongly in our opinion), since the large and small non-coherent height fluctuations have a similar behavior and a length of the same order. The origin of these non-coherent film height fluctuations is not clear at the moment. They could perhaps be associated to the effect of the large-scale turbulence structures in the gas flow on the film.

The disturbance waves are the most striking interfacial structures in the figures discussed above. They have probably the largest contribution to the interfacial friction due to their three-dimensional character and their large height fluctuations (this point is developed further in Belt et al. (2009)). Therefore, in this study we will mainly focus on the characterization of the disturbance waves.

4. Experimental determination of the disturbance waves

In the statistics of the disturbance waves, the non-coherent structures must not be accounted for. Therefore, to obtain unbiased statistics, a robust procedure is needed to determine all and only the disturbance waves from the time-signal of the film thickness (Azzopardi, 1986). It is clear from the time-signal in Fig. 12 that a simple threshold will not be sufficient in separating the coherent disturbance waves from the non-coherent structures, as the non-coherent structures have sometimes a similar height to the disturbance waves. Since disturbance waves are primarily characterized by a correlation in the streamwise direction with an approximately constant propagation velocity, whereas the non-coherent structures are not, we used here this criterion to determine the disturbance waves. The disturbance waves are determined in three steps. First, the potential disturbance waves are listed: using a threshold on the time-signal of the film thickness, the events higher than the threshold are considered as potential disturbance waves. Then, in two next steps, the large non-coherent structures are removed from this set of potential disturbance waves, using mainly the correlation in the streamwise direction.

Since the non-coherent structures often have an amplitude significantly smaller than that of the disturbance waves, using a correct threshold, a large part of the non-coherent structures can be separated from the actual disturbance waves in the first step. The correct amplitude of the threshold is chosen by considering the total amount of waves as a function of the threshold, see Fig. 13. We can assume that the small non-coherent structures have an height that varies randomly. Therefore, the amount of small non-coherent structures behaves like a Poisson distribution when increasing the amplitude of the threshold. With a significant separation in the height of the disturbance waves and the small non-coherent structures, above a certain threshold, the amount of "waves" will decrease more slowly, since the actual disturbance waves do not obey to this Poisson distribution. This amplitude of the threshold is used, but reduced by 50% to ensure that all disturbance waves are accounted for, in order to perform a first crude separation between the disturbance waves and non-coherent structures.

Due to the large fluctuations in the height of the disturbance wave, or to a local disruption in the shape of the disturbance wave, some waves exhibit two sharp peaks within a very short time-interval. When considering the evolution in space of such a wave (i.e. when comparing the time-signals at different positions in the streamwise direction), we can see that the two peaks merge into one peak. Therefore, the two peaks must not be considered as individual distinct waves. However, the two peaks will both have a good cross-correlation with the corresponding disturbance wave at other axial locations. To solve this, in the second step, we apply to the set of potential disturbance waves a "dead-time" (i.e. a short time-interval after the occurrence of a wave, in which no other wave can occur), in order to remove the multiple validation of a single wave. This is similar to the multiple validation in Laser Doppler Anemometry (e.g. Van Maanen, 1999). In this study, we use in the post-processing a dead-time between 10^{-2} s (for $U_{GS} = 42$ m/s) and 2×10^{-2} s (for $U_{GS} = 22$ m/s), which corresponds to about half the time needed for the disturbance wave to flow over a pair of electrodes of the film thickness probe.

In the third step, we use the correlation to determine the disturbance waves from the events above the threshold: an event in the

time-signal is accepted if a similar event is observed in the time-signals at all other streamwise positions, but shifted in accordance with the mean wave velocity. For instance, for the event at time t and position (θ, z) to be accepted as a disturbance wave, a similar event at position $(\theta, z+d)$ must occur in the window on the time-signal between $t + d/C_W - \Delta/2$ and $t + d/C_W + \Delta/2$, where C_W is the mean velocity of the disturbance waves (obtained from the cross-correlation between the positions (θ, z) and $(\theta, z+d)$), and Δ the window size. The window size is taken here equal to the dead-time used in the second step. In this way, a clean set of disturbance waves is obtained at each position (θ, z).

5. Results

The statistical properties are obtained for each measurement from a time-signal of 119 s in total. This means, for the disturbance wave properties, about 350 disturbance waves (for the lowest gas and liquid superficial velocities) to 1400 disturbance waves (for the highest gas and liquid superficial velocities) are accounted for. Furthermore, since the vertical annular flow is assumed (i) fully-developed, and (ii) axisymmetric, all 320 measurement locations are used in calculating the mean properties in the vertical annular flow. It is checked that the statistics do not differ significantly from point to point along the circumference, which means that the pipe is carefully aligned with the vertical. We note that the axisymmetry of the flow is an important condition, since the behavior of the disturbance waves is non-linear with the base film thickness, and therefore averaging in the circumferential direction can only be done if the base film has a constant thickness, i.e. if it is axisymmetric. Furthermore, we note that it has been observed in preliminary measurements that a small misalignment of the pipe with the vertical induces a clear asymmetry in the mean film thickness. This shows that a careful alignment of the pipe with the vertical is needed.

In this section, we show probability density functions (pdf) for properties of the disturbance waves. Note that, by definition, the integral of a pdf is equal to one.

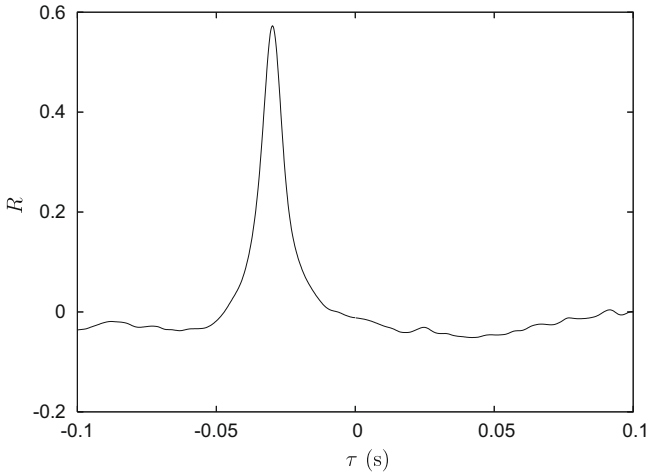

Fig. 16. Cross-correlation function of the film thickness measured at the first and fifth axial location, for U_{GS} = 42 m/s and U_{LS} = 0.02 m/s.

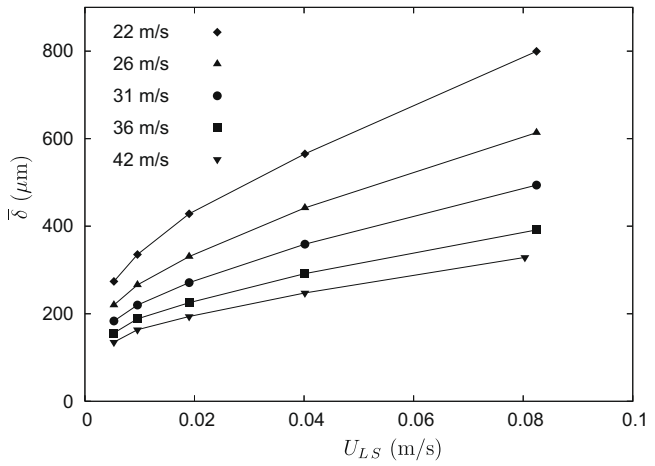

Fig. 14. Mean film thickness $\bar{\delta}$ as a function of the liquid superficial velocity U_{LS}, for different gas superficial velocities U_{GS}.

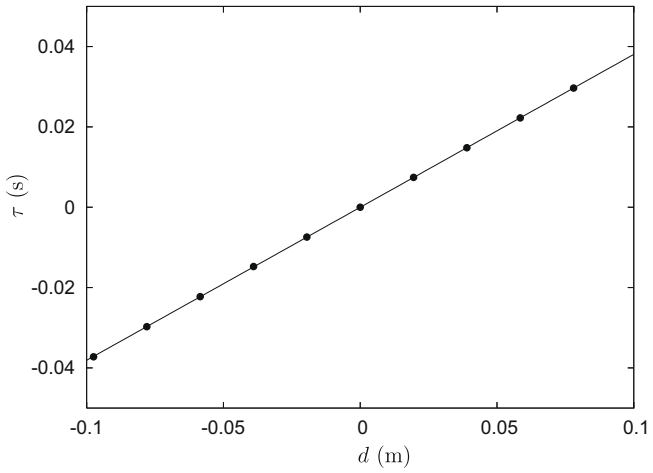

Fig. 17. Time-delay corresponding to the maximum cross-correlation as a function of the axial distance separating the two measurement locations. The reference measurement location is halfway the sensor. The slope corresponds to the inverse of the interfacial velocity $1/C_W$. For U_{GS} = 42 m/s and U_{LS} = 0.02 m/s.

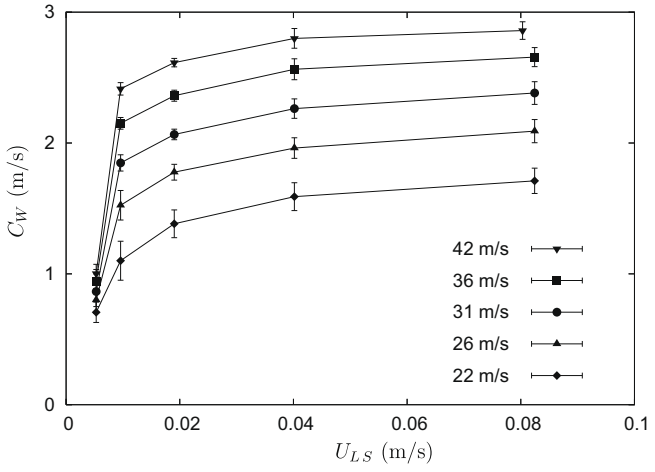

Fig. 15. Mean interfacial velocity C_W in the laboratory reference frame as a function of the liquid superficial velocity U_{LS}, for different gas superficial velocities U_{GS}. The error bars correspond to once the standard deviation of the interfacial velocity.

5.1. Mean film thickness and mean wave velocity

In Figs. 14 and 15, we show the mean film thickness $\bar{\delta}$ and the wave velocity C_W in the laboratory reference frame, respectively.

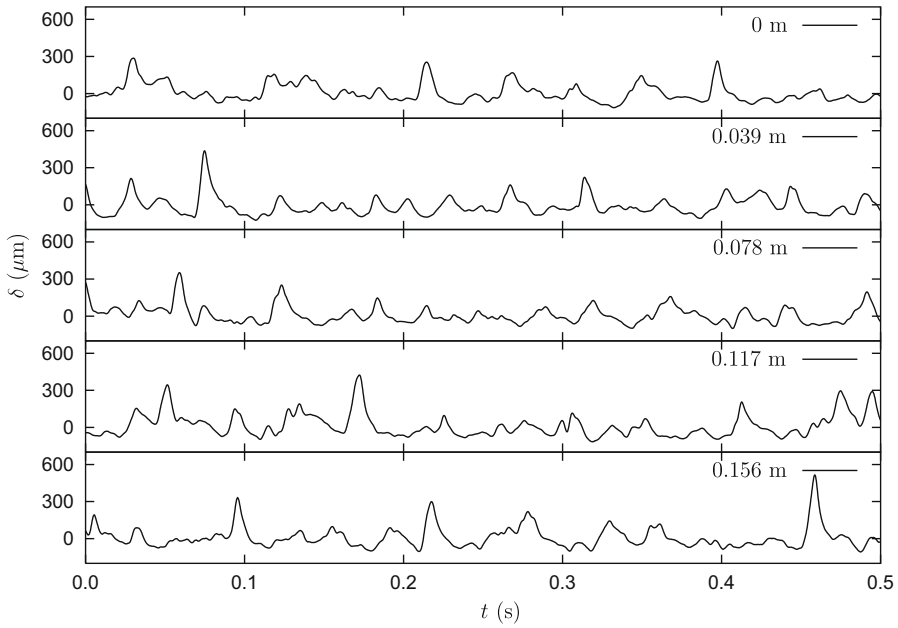

Fig. 18. Time-signal of the film thickness at different axial positions for one given circumferential position. The mean film thickness has been subtracted from the time-signals. The liquid and gas superficial velocities are equal to U_{LS} = 0.005 m/s and U_{GS} = 26 m/s, respectively. The mean film height is equal to 220 μm.

As could be expected from the mass balance of the film, we can see in Fig. 14 that the mean film thickness $\bar{\delta}$ increases with the liquid superficial velocity U_{LS}, and decreases with the gas superficial velocity U_{GS}. We can also see that Fig. 14 shows a parabolic behavior ($\bar{\delta}^2 \sim U_{LS}$) for very small liquid superficial velocities, as we should obtain. Indeed, for $U_{LS} = 0$, we have $\bar{\delta} = 0$. Furthermore, by definition, we have $U_{LS} \approx 4U_{LF}\bar{\delta}/D$, where U_{LF} is the mean velocity in the film, which for very small liquid superficial velocities can be assumed proportional to the mean film thickness $\bar{\delta}$ (laminar Couette flow). Hence, for very small U_{LS}, we expect that U_{LS} varies as $\bar{\delta}^2$, which trend can indeed be observed in Fig. 14.

The interfacial velocity C_W in Fig. 15 is calculated using the cross-correlation between the time-signals measured at one reference axial location and at all other axial locations, for the same circumferential position. The interfacial velocity C_W is defined as the ratio of the distance between the two measurement locations and the time-delay corresponding to the maximum cross-correlation. Then, the average and standard deviation of the interfacial velocity is obtained from the 9×32 data points. A typical example of the cross-correlation function is shown in Fig. 16. We can see that the peak in the cross-correlation is sharp, the width of the peak being similar to that of the autocorrelation function (which is shown below in Fig. 23). This suggests that the large structures flow over the film with a quasi-constant velocity, and that their dispersion is negligible. In Fig. 17, we show the time-delay corresponding to the maximum cross-correlation as a function of the axial distance separating the two measurement locations. The slope in Fig. 17 corresponds to the inverse of the velocity of the large structures on the film. Since a linear function can be fitted to Fig. 17, it means that the velocity of the structures on the film is roughly constant.

For Re_{LS} larger than Re_{LS}^{crit}, the disturbance waves have the largest contribution to the cross-correlation, since they are frequent, coherent and have the largest height. Therefore, the measured interfacial velocity C_W corresponds to the characteristic velocity of the disturbance waves. Note that this velocity is larger than that of the interface in between the disturbance waves. For Re_{LS} smaller than Re_{LS}^{crit}, non-coherent height fluctuations mainly cover the interface. These fluctuations can be quite large, sometimes in the order of the disturbance wave height, however, it seems that they cannot become coherent in order to become "disturbance" waves. Indeed, this can be observed in Fig. 18, which shows for this regime time-signals of the film thickness measured at different axial positions for one given circumferential position. In Fig. 18, the first large structure which is coherent in the axial direction corresponds to a disturbance wave, showing that some disturbance waves occur, although not frequently. Fig. 18 also shows many height fluctuations which have a similar amplitude to the disturbance wave, however, they are not coherent in the axial direction (and neither in the circumferential direction, as can be observed from the time-signals at different circumferential positions, not shown here). From this, it is clear that the interface is not necessarily smooth for Re_{LS} smaller than Re_{LS}^{crit}, especially at the lowest gas superficial velocities of our experiments. Although the lifetime of the non-coherent height fluctuations is limited, they still have a correlation during their lifetime. Hence, for these Re_{LS}, C_W is a measure for the velocity of the non-coherent height fluctuations, which is probably not very different from the actual velocity of the interface.

We can see in Fig. 15 that the interfacial velocity C_W tends to an asymptotic value when the liquid superficial velocity U_{LS} increases. In between the two lowest liquid superficial velocities U_{LS}, the interfacial velocity C_W decreases sharply. Since the velocity of the disturbance waves is larger than that of the base film, this decrease can be explained by the occurrence or not of the disturbance waves, depending on the value of Re_{LS} compared to Re_{LS}^{crit}. Furthermore, the interfacial velocity C_W increases roughly linearly with the superficial gas velocity U_{GS}.

Marmottant and Villermaux (2004) performed a theoretical study on co-axial jets, which configuration is in fact very similar to that of annular flow. They showed that a shear instability governs the large waves on the jet. The linear shear instability analysis provides an equation for the wave velocity C_W:

$$C_W = \frac{\sqrt{\rho_G}U_G + \sqrt{\rho_L}U_{LF}}{\sqrt{\rho_G} + \sqrt{\rho_L}} \tag{3}$$

in the laboratory reference frame, with U_G the gas velocity in the gas core. This equation is obtained when the assumption $U_G \gg U_{LF}$ is

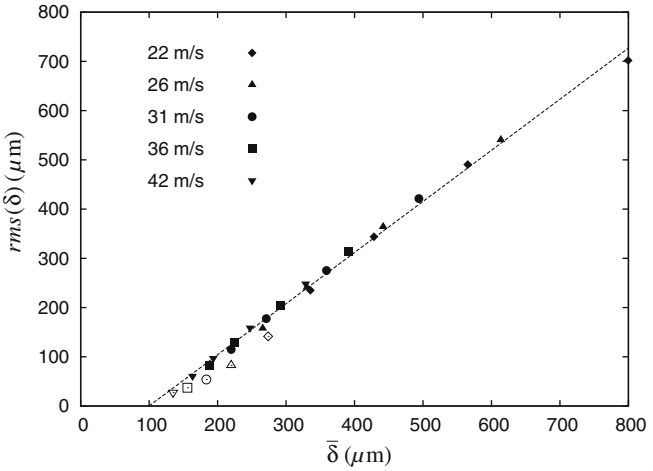

Fig. 19. Standard deviation of the film thickness $rms(\delta)$ as a function of the mean film thickness $\bar{\delta}$. The closed symbols correspond to a wavy interface, the open ones to liquid mass-flow rates $\dot{M}_L$ for which the interface is quasi-smooth (i.e. no disturbance waves, or disturbance waves that start to appear). The dashed line corresponds to a linear fit of the closed symbols, which slope is equal to 1.04.

made in the analysis. Note that an almost identical equation has been proposed by Pearce (Azzopardi, 1986). Thus, this equation predicts the linear relationship between C_W and U_{GS} which is observed experimentally, as U_G is close to U_{GS}. Eq. (3) has been tested on our experimental data. A good agreement is found, with an error on the predicted wave velocity smaller than ±20% of the experimental wave velocity, except for the highest liquid film velocities for which the predicted wave velocity is too high. Note that the latter cases occur for $U_G \approx 15\ U_{LF}$, so the assumption $U_G \gg U_{LF}$ is not completely verified. It could be interesting as a future work to see whether the shear instability analysis performed by Marmottant and Villermaux (2004) applies to annular flow, since, if it applies, it would provide useful information on the disturbance waves.

In Fig. 19, we show the standard deviation of the film thickness $rms(\delta)$ as a function of the mean film thickness $\bar{\delta}$. Note that $rms(\delta)$ does not correspond to the error, but to a statistical representation of the film height variations. We can see in Fig. 19 a linear dependence between $rms(\delta)$ and $\bar{\delta}$ for the different gas and liquid superficial velocities with Re_{LS} larger than Re_{LS}^{crit} (the closed symbols). For Re_{LS} smaller than Re_{LS}^{crit} (the open symbols), the standard deviation is slightly below that linear relationship. From the time-signals, it is clear that for Re_{LS} larger than Re_{LS}^{crit} the disturbance waves have the largest contribution to the standard deviation. For Re_{LS} smaller than Re_{LS}^{crit}, the standard deviation results mainly from the non-coherent height fluctuations, as it can be seen in Fig. 18. The fact that the standard deviation is not much smaller shows that this regime corresponds to a transition regime, in which the disturbance waves are not stable, and therefore are referred to as large non-coherent height fluctuations. In other words, the large non-coherent fluctuations could be seen as developing disturbance waves, as it was proposed in Wolf et al. (1996). However, for Re_{LS} smaller than Re_{LS}^{crit}, those large non-coherent height fluctuations cannot become stable.

The physical reason behind the linear relationship in Fig. 19 is not understood at the moment by the authors. In Chu and Dukler (1975), it is also noted that the mean film thickness and the standard deviation are of the same order of magnitude. Practically, the linear relationship can be used to define the interfacial friction factor as a function of the mean film thickness $\bar{\delta}$, as it is done in the Wallis correlation (Wallis, 1969), instead of its standard deviation $rms(\delta)$, which characterizes the height of the interfacial roughness elements.

5.2. Verification of the experimental results

Below, we will compare our experimental mean film thickness $\bar{\delta}$ and mean wave velocity C_W with predictions, in the case the predictions are straightforward. Also, we will compare these results with those of Fore and Dukler (1995), which are obtained at similar conditions in a pipe of almost the same diameter and with the same fluids.

For a vertical annular flow, in the case of very small liquid flow rates, the mean film thickness $\bar{\delta}$ and the mean wave velocity C_W can be predicted easily. For instance, the Reynolds number of the film Re_F (defined as $U_{LF}\bar{\delta}/\nu_L$) can be sufficiently low, such that the film may be assumed laminar. In that case, large disturbance waves do not exist on the interface (Azzopardi, 1997). Then, the entrainment of droplets from the film into the gas core is negligible (Azzopardi, 1997; Fore and Dukler, 1995), and the liquid mass-flow rate in the pipe $\dot{M}_L$ equals the mass-flow rate in the film $\dot{M}_{LF}$. The wave velocity C_W, obtained from the cross-correlation of time-signals at different axial locations, corresponds to the velocity of the small non-coherent height fluctuations, and is probably not very different from the actual velocity of the interface. Hence, in this case of very small liquid flow rates, the momentum balances in the axial direction of the gas core and of the liquid film can be simplified significantly.

From the momentum balance in the vertical direction on the fully-developed liquid film, assuming that (i) there is no entrainment, therefore, no advection of momentum due to the atomization and deposition of droplets (Fore and Dukler, 1995), and (ii) the liquid film is laminar, the velocity profile $u(y)$ inside the film can be derived:

$$u(y) = \frac{\tau_i}{\mu_L} y + \frac{1}{\mu_L}\left(-\frac{dP}{dz} - \rho_L g\right)\left(\bar{\delta} - \frac{y}{2}\right) y \tag{4}$$

where y is the distance from wall, z the vertical coordinate, τ_i the interfacial shear-stress (in the positive vertical direction), $-dP/dz$ the pressure-gradient in the vertical direction, μ_L the dynamic viscosity, ρ_L the density of the liquid, and g the gravitational acceleration. For simplicity, the equation is shown in Cartesian coordinates, i.e. by opening up the pipe and neglecting the curvature. However, we verified that the results obtained with the equations in cylindrical coordinates are quasi the same (the predicted mean film thickness differs less than 1 μm). The measured "wave" velocity C_W is roughly equal to $u(\bar{\delta})$.

The continuity equation on the liquid film provides a second equation between the velocity u, the mean film thickness $\bar{\delta}$ and the mass-flow rate of liquid $\dot{M}_L$. In Cartesian coordinates, it is:

$$\dot{M}_L = \rho_L \int_0^{\bar{\delta}} u(y)\pi D\, dy \tag{5}$$

Hence, the mean film thickness $\bar{\delta}$ and the velocity at the interface $u(\bar{\delta})$ can be calculated using the momentum balance and the continuity equation in the film, if the liquid mass-flow rate $\dot{M}_L$, the pressure-gradient $-dP/dz$ and the interfacial shear-stress τ_i are known.

Table 2
Comparison between the measurement and the prediction of the mean film thickness $\bar{\delta}$ and the interfacial velocity C_W. Values for the film thickness are in μm, values for the interfacial velocity in m/s. Re_F and Re_G correspond to, respectively, the Reynolds number in the film and the Reynolds number of the gas core, which is defined as $U_G(D-2\bar{\delta})/\nu_G$. The subscript "pred" corresponds to the predicted values. The subscript "Fore" corresponds to interpolated values from the data in Fore and Dukler (1995) to the same conditions of the measurements here.

Re_{LS}	Re_G	Re_F	$\bar{\delta}$	$rms(\delta)$	C_W	$\bar{\delta}_{pred}$	$u(\bar{\delta})_{pred}$	$\bar{\delta}_{Fore}$
238	143×10^3	60	138	33	1.01	153	0.90	206
238	124×10^3	60	157	44	0.94	179	0.78	232

The first two values are measured and the interfacial shear-stress τ_i is estimated using the momentum balance in the axial direction of the gas core. Since there is no convection of momentum due to the entrainment of droplets (Fore and Dukler, 1995), the axial momentum balance of the gas core is simplified into:

$$-\frac{dP}{dz} - \rho_G g - \tau_i \frac{4}{D - 2\bar{\delta}} = 0 \tag{6}$$

where ρ_G is the density of the gas. Solving the three equations gives the predicted mean film thickness $\bar{\delta}$ and the velocity at the interface $u(\bar{\delta})$.

We compare the predictions of the mean film thickness $\bar{\delta}$ and the velocity at the interface $u(\bar{\delta})$ with the experimental values in Table 2 at the lowest liquid superficial velocity U_{LS} and the two highest gas superficial velocities U_{GS} of the measurements. At these conditions, we verified that almost no large disturbance waves are found. Furthermore, the non-coherent height fluctuations are relatively small (see also Fig. 19). However, at the lowest U_{GS} in Table 2, some disturbance waves start to appear and the non-coherent height fluctuations become larger. For this reason, no predictions are done for lower Re_G, since the assumptions made start to be false. In Table 2, we also show the Reynolds number of the film Re_F, which is very small, and much smaller than the Reynolds number at which a boundary layer starts to become turbulent (equal to ≈520, according to Schlichting (1979)). Therefore, the assumption made of a laminar velocity profile in the liquid film is probably valid for the situations in Table 2.

We can see from Table 2 that the differences between our measurements and the predictions of the mean film thickness $\bar{\delta}$ and the interfacial velocity $u(\bar{\delta})$ are small, taken into account the assumptions made (i.e. the laminar flow in the film) and the accuracy of the measurements of the pressure-gradient $-dP/dz$, the mass-flow rates of water and air $\dot{M}_L$ and $\dot{M}_G$, and the film thickness $\bar{\delta}$. The difference between the measurements and predictions of $\bar{\delta}$ is roughly equal to the measurement error $e(\bar{\delta})$ in the mean film thickness. Furthermore, we can see that the measured mean film thickness $\bar{\delta}$ is about 10% smaller than the predicted one, whereas the measured interfacial velocity $u(\bar{\delta})$ is about 10% larger than the predicted one, i.e. the differences are in agreement with the continuity equation. Therefore, we can conclude that the results of the measurement technique are in reasonable agreement with the predictions.

We also compared our experimental results with those of Fore and Dukler (1995), which are obtained at similar conditions in a pipe of almost the same diameter and with the same fluids. From Table 2, we can see that the differences between the predictions and the measurements of Fore and Dukler (1995) are larger compared to our results. The entire set of mean film thickness $\bar{\delta}$ and wave velocity C_W obtained in this study has been compared with the measurements of Fore and Dukler (1995) (i.e. also with a wavy interface). We have a similar trend in the behavior of the mean film thickness $\bar{\delta}$ and of the wave velocity C_W as a function of the water and air flow-rates. However, we find again quantitative differences in $\bar{\delta}$ and C_W. The differences in the mean film thickness could be caused by an error in the measurement technique or calibration in the present work or in that of Fore and Dukler (1995). However, the wave velocity depends only on the signal fluctuations and not on the magnitude, and, therefore, is less likely to be measured wrongly. The differences might be attributed to the relatively short developing length for the liquid film in Fore and Dukler (1995), which is equal to $69 \cdot D$, instead of $130 \cdot D$ here. We also note that, for very low liquid flow-rates as in Table 2, the film thickness measurement technique used by Fore and Dukler (1995) could lead to an overestimation of the mean film thickness $\bar{\delta}$. For instance, in Fore and Dukler (1995), the film thickness is measured through the conductance between two parallel wires protruding through the film. Since the diameter of their wires is approximately half of the film thickness at the conditions of Table 2, the wires could induce a local displacement of the liquid film due to surface tension and therefore increase the film thickness.

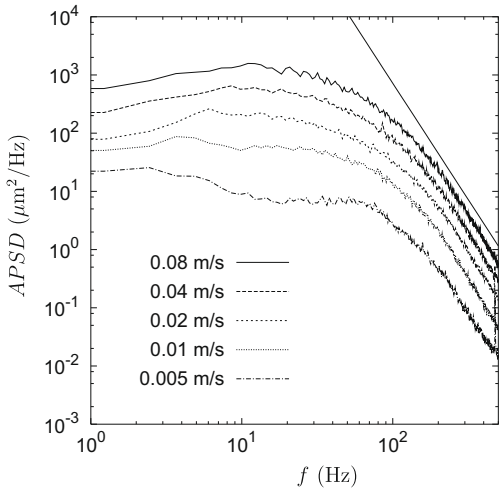

Fig. 20. Auto-power spectrum density for a large range of frequency f, for the highest gas superficial velocity U_{GS} and for different liquid superficial velocities U_{LS}. The "linear" solid line corresponds to a logarithmic slope of −4.

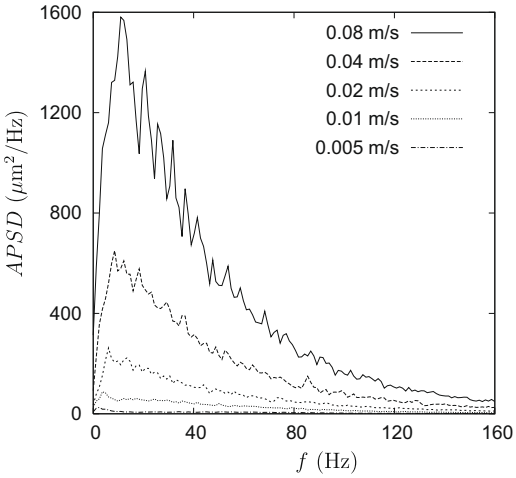

Fig. 21. Auto-power spectrum density for a small range of frequency f, for the highest gas superficial velocity U_{GS} and for different liquid superficial velocities U_{LS}.

5.3. Global characterization of the waves

The interfacial waviness is usually described in the literature on annular flow using the auto-power spectrum density (in frequency–space). Here, we calculated the (mean square amplitude) power spectra by windowing the data using a Bartlett window in 140 segments of about 1 s. Therefore, the standard deviation of the spectral estimate at f will be about 8.5% of the value. In Figs. 20 and 21, we show the auto-power spectrum density, for a large and small range of frequencies, respectively, and for different liquid superficial velocities U_{LS} at the gas superficial velocity U_{GS} equal to 42 m/s. We can see in Figs. 20 and 21 that the shape of the power spectra is quite similar for the different liquid superficial velocities U_{LS}, except for the lowest U_{LS}, for which no disturbance waves exist at the interface. The power contained in the signal is largest for the highest U_{LS}, meaning that the waves are also largest

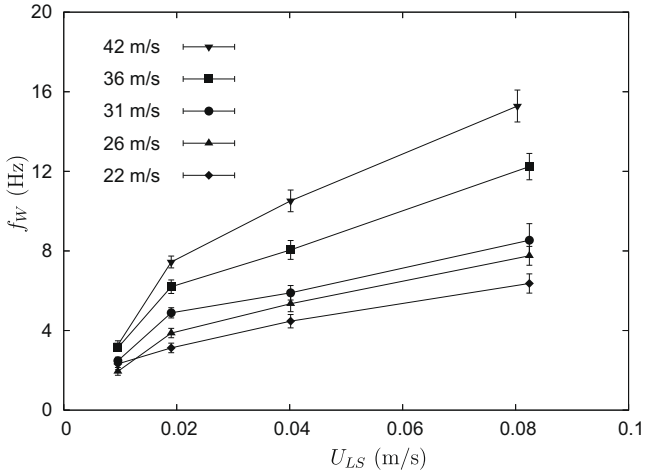

Fig. 22. Mean frequency of the disturbance waves f_W as a function of the liquid superficial velocity U_{LS}, for different superficial gas velocities U_{GS}. The error bars correspond to once the standard deviation.

for the highest U_{LS}. In Fig. 21, we can see that most of the energy is contained in frequencies lower than ≈50 Hz. The frequency corresponding to the maximum in energy ranges between 3 and 12 Hz. These values correspond to the measured frequency of the disturbance waves f_W obtained by counting the coherent waves using the detection algorithm described above. The mean frequency of the disturbance waves is shown in Fig. 22. The maximum in energy shifts to higher frequencies for the higher liquid superficial velocities U_{LS}, meaning that the frequency of the disturbance waves is larger for higher U_{LS}.

In Fig. 20, we can see that, for $f \gtrsim 200$ Hz, the energy decreases with a power approximately equal to -4, for all liquid superficial velocities U_{LS}, i.e. also when no disturbance waves flow over the interface. The latter decay could be linked to the non-coherent height fluctuations on the interface. We note that Chu and Dukler (1975) also observed such a decrease in the power spectrum for downward co-current annular flow. Furthermore, in the literature on wind-generated gravity waves (Phillips, 1985), a logarithmic slope of -4 has also been found. This similarity could be investigated further to see whether the existing theory on wind-generated gravity waves on oceans could be used in annular flow to characterize the non-coherent height fluctuations.

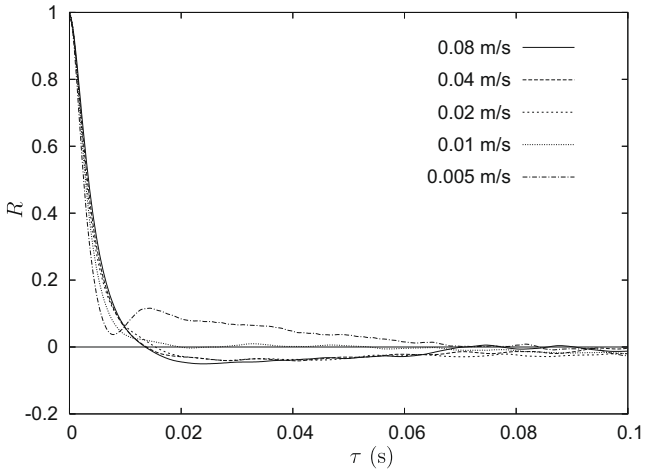

Fig. 23. Autocorrelation function of the film thickness, for the highest gas superficial velocity U_{GS} and for different liquid superficial velocities U_{LS}.

From the time-signal of the film thickness, the wave structure seems intermittent. From the auto-power spectrum densities presented in Figs. 20 and 21, however, we cannot draw conclusions on the wave structure in space. In Fig. 23, we show the time-autocorrelation function, for the different liquid superficial velocities U_{LS} at the highest gas superficial velocity (note that the time-autocorrelation at different gas superficial velocities have a similar shape, except that the time-delay at the crossing through zero increases with decreasing gas superficial velocities). This figure shows that the autocorrelation function decreases very quickly to zero. Apparently, the signal does not show any correlation or periodicity. The correlation at very small time delays ($\tau \lesssim 0.015$ s for the cases considered in Fig. 23) corresponds to the finite length of the waves. For instance, using the wave velocity C_W and the first crossing through zero in the time-autocorrelation, a characteristic wave length can be calculated. For the different liquid superficial velocities U_{LS}, except the lowest one, we obtain a characteristic length between 0.04 and 0.05 m. Below, when presenting the properties of the disturbance waves, we will see that this characteristic length corresponds to the length of the disturbance waves, which is roughly equal to the pipe diameter $D = 0.05$ m and independent of the liquid and gas superficial velocities.

The fast decrease to zero in the autocorrelation function could suggest that the disturbance waves are randomly distributed in time at one location, i.e. in space because of the constant velocity of the disturbance waves. To verify this assumption, we can measure the probability density function of the "time-between-waves", by analogy to the work on Laser Doppler Anemometry (e.g. Van Maanen, 1999). This is done in the next section.

5.4. Spatial distribution of the disturbance waves

The disturbance waves are determined from the time-signals as explained in Section 4. Then, the probability density function of the time in between two successive waves can be determined, which is shown in Fig. 24, for different liquid superficial velocities U_{LS} at the highest gas superficial velocity $U_{GS} \approx 42$ m/s. The data at the lowest liquid superficial velocity U_{LS} (corresponding to $Re_{LS} = 238$) are not shown since almost no disturbance waves exist on the interface at that Re_{LS}. From Fig. 24, we can see that the pdf p of the time-between-waves can be very well fitted to a Gamma distribution:

$$p(t^*) = \frac{n^n}{\Gamma(n)} t^{*n-1} e^{-nt^*} \tag{7}$$

where the order n is a constant, and t^* the time-between-waves made dimensionless with its mean, i.e. $1/f_W$ with f_W the mean frequency of the disturbance waves. As a result, the temporal distribution of the disturbance waves can be described using the disturbance wave frequency, and the order n as only parameter. Since the wave velocity is roughly constant for all disturbance waves for a given U_{GS} and U_{LS}, the spatial distribution of the disturbance waves is proportional to the temporal distribution. Moreover, in Fig. 24, the order n of the Gamma distribution is an integer. The order increases with lower liquid superficial velocities U_{LS}, but appears to be independent of the gas superficial velocity U_{GS}, as can be seen from Fig. 25. We note, however, that the pdf of the time-between-waves changes at lower gas superficial velocities U_{GS}, due to the frequency f_W of the disturbance waves (see the equation of the Gamma distribution).

The Gamma distribution of order n is obtained as an n-convolution of independent and random exponential distributions (Feller, 1971). Physically, a Gamma distribution can be observed for the pdf of the droplet diameters obtained from ligament break-up in jets (Marmottant and Villermaux, 2004). Since we also observed a Gamma distribution for the spacing-between-waves, by analogy

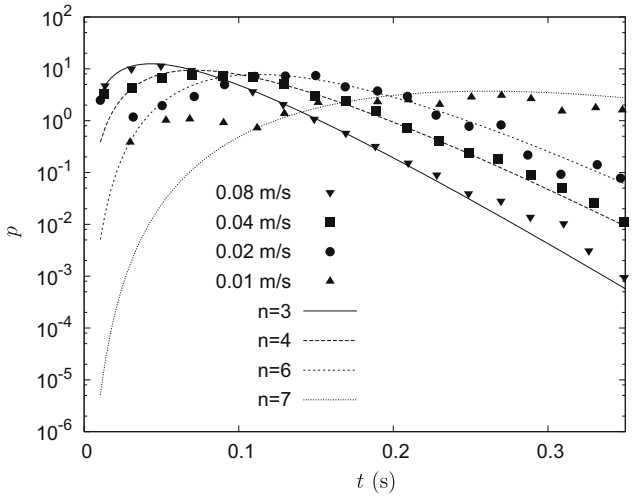

Fig. 24. Probability density function p of the time-between-waves t, for different liquid superficial velocities U_{LS} at the highest gas superficial velocity U_{GS} = 42 m/s. The closed symbols correspond to the measured pdf, and the lines to the Gamma distributions fitted to the measurements, with the order n an integer.

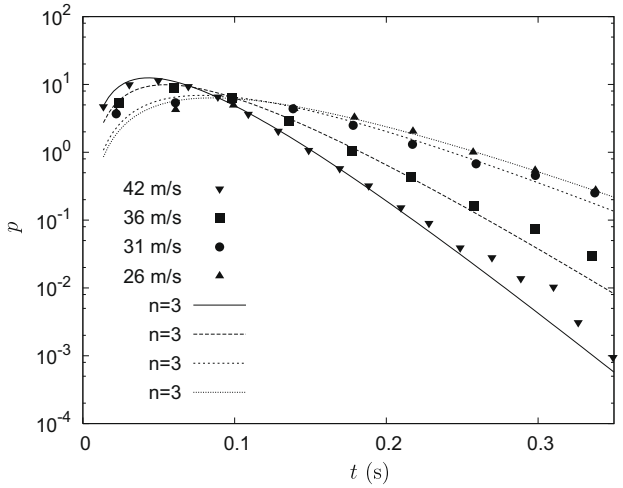

Fig. 25. Probability density function p of the time-between-waves t, for different gas superficial velocities U_{GS} at the highest liquid superficial velocity U_{LS} = 0.08 m/s. The closed symbols correspond to the measured pdf, and the lines to the Gamma distributions fitted to the measurements, with the order n an integer.

to the formation of the droplet distribution in sprays, a mechanism for the disturbance wave formation can be proposed.

A perturbation of the interface is a precursor to the formation of a disturbance wave, and is probably due to the turbulent gas flow. In the early stage of the disturbance waves formation, the perturbations can be assumed to be located randomly over the interface, due to the nature of the turbulent gas flow. Hence, in the initial stage, the exponential (Poisson) distribution is the most probable shape for the spacing-between-waves distribution. During their growth, the perturbations can interact with the gas flow (e.g. damping or deformation by the gas flow), and with each other (e.g. coalescence or continuity effects in the liquid film). Provided the interactions occur randomly, their cascade leads the spacing-between-waves distribution to evolve to a stable distribution by self-convolution. The n-self-convolution of an exponential distribution is precisely the Gamma distribution, which is observed in our experiments. We note that the order n of the spacing-between-waves distribution is independent of U_{GS} and dependent of U_{LS}, hence, it suggests that the final stable spatial distribution of the disturbance waves is determined by random interactions between the perturbations, e.g. by coalescence, and not by the interaction of the gas flow with the perturbations.

From a practical point of view, disturbance waves are events randomly distributed in space. Since it can be expected that the disturbance waves have the largest contribution to the interfacial friction, the random spatial distribution of the disturbance waves suggests that the interfacial friction could be described by the theory on random "K" roughness in single-phase turbulent pipe flows. This point has been developed further in Belt et al. (2009).

5.5. Mean properties of the disturbance waves

Since the unbiased set of disturbance waves can be detected using the algorithm described in Section 4, we can now describe the shape of individual disturbance waves and obtain unbiased statistics. Below, we will show some mean properties describing the disturbance waves, such as their height and length. We define here the height of the disturbance wave h_W as the distance between the top of the disturbance wave and the mean film thickness $\bar{\delta}$. The definition of the length of the disturbance wave l_W is much more arbitrary (see the time-signals in Figs. 8–10). Here, we define the length of the disturbance wave l_W as the length between the two

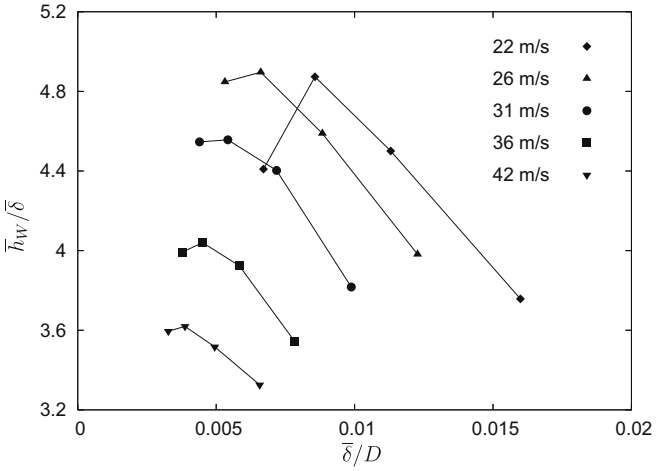

Fig. 26. Ratio of the mean height of the disturbance waves $\bar{h}_W$ to the mean film thickness $\bar{\delta}$ as a function of the mean film thickness. Each line between the solid points corresponds to different liquid superficial velocities U_{LS} at one superficial gas velocity U_{GS}.

first minima enclosing the maximum of the disturbance wave which are below the mean film thickness $\bar{\delta}$. We note that using the two first minima around the maximum (i.e. without the condition below the mean film thickness) to determine the length of the wave would underestimate its actual size, because of the height fluctuations on the disturbance wave (Paras and Karabelas, 1991).

Fig. 26 shows the ratio between the mean height of the disturbance waves $\bar{h}_W$ and the mean film thickness $\bar{\delta}$, as a function of $\bar{\delta}$. The ratio is close to 4, as suggested in the literature. However, we can see that the values can differ from 4 by as much as 25%. Furthermore, it is not a function of the mean film thickness $\bar{\delta}$ only. Especially, the ratio tends to be smaller than 4 for the highest gas superficial velocities U_{GS}, and larger than 4 for the lowest U_{GS}. We note that the ratio $\bar{h}_W/\bar{\delta}$ shows a different trend for U_{GS} = 22 m/s compared to the other gas superficial velocities. However, it has been verified that the set of disturbance waves for U_{GS} = 22 m/s is correctly determined, and the different trend could perhaps be linked to the start of flow reversal around that value of the gas superficial velocity.

In Fig. 27, we show the pdf of the wave height h_W, for the four different liquid superficial velocities U_{LS} at the highest gas superfi-

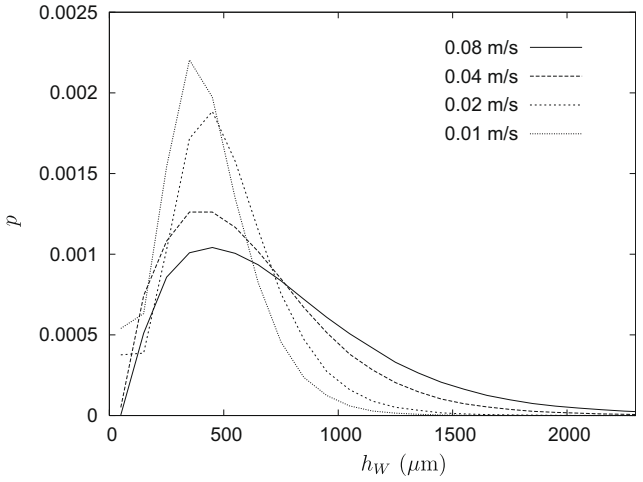

Fig. 27. Probability density function p of the wave height h_W, for different liquid superficial velocities U_{LS} at the gas superficial velocity U_{GS} = 42 m/s.

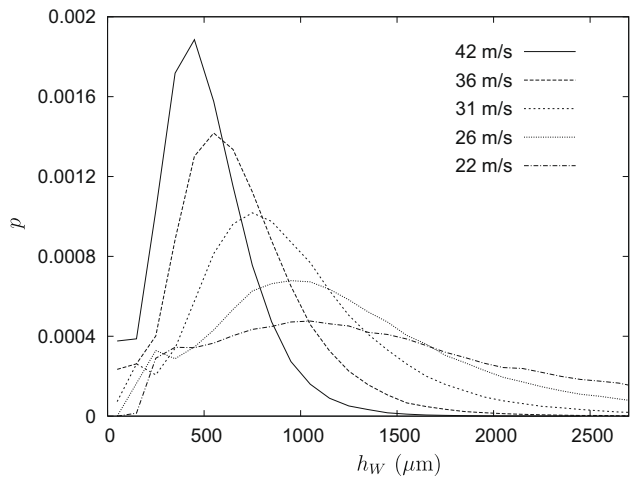

Fig. 28. Probability density function p of the wave height h_W, for different gas superficial velocities U_{GS} at the liquid superficial velocity U_{LS} = 0.02 m/s.

cial velocity U_{GS} = 42 m/s. We can see that the most probable wave height is about the same for the different liquid superficial velocities U_{LS}. However, the exponential decay of the pdf to larger wave heights is smaller for the larger liquid superficial velocities U_{LS}. As a result, the pdf of the height of the disturbance waves is much broader for the larger liquid superficial velocities U_{LS}, giving a larger mean height of the disturbance waves $\bar{h}_W$. We note that, for the two smallest liquid superficial velocities U_{LS}, a small amount of non-coherent height fluctuations are contained in the pdf of the disturbance wave height, which can be observed by the change in the slope of the pdf for very small heights. However, the amount of non-coherent height fluctuations is small compared to the amount of disturbance waves in the pdf of the wave height, and is not expected to have a strong effect on the calculated mean quantities. This validates a posteriori the detection algorithm of the disturbance waves. In Fig. 28, we show the pdf of the wave height h_W, for different gas superficial velocities U_{GS} at a liquid superficial velocity U_{LS} equal to 0.02 m/s. We can see that the maximum probability for the wave height, which is approximately independent of the liquid superficial velocity U_{LS}, now increases to larger wave heights for lower gas superficial velocities U_{GS}. Also, the exponential decay from the maximum to larger wave heights h_W is lower for the lower gas superficial velocities U_{GS}, making the pdf much broader for the lower U_{GS}. Again we can see that, at small wave heights, a small amount of non-coherent height fluctuations is counted as disturbance waves.

In Fig. 29, we show the mean length of the disturbance waves $\bar{l}_W$, for the different liquid and gas superficial velocities. In all cases, the mean length of the disturbance waves $\bar{l}_W$ is slightly larger than the pipe diameter and ranges mainly between 0.05 and 0.06 m. So, the mean length $\bar{l}_W$ appears to be more or less independent of the superficial velocities U_{GS} and U_{LS}. It is remarkable that the length of the disturbance waves is very close to the pipe diameter D. However, we do not have an explanation for this observation.

The pdf of the length of the disturbance waves is shown in Figs. 30 and 31, the first for different liquid superficial velocities U_{LS} at the highest gas superficial velocity U_{GS} = 42 m/s, and the second for different gas superficial velocities U_{GS} at the highest liquid superficial velocity U_{LS} = 0.08 m/s. We can see that the pdf are similar for all measurements. The maximum of the pdf corresponds to a length of about 0.04–0.05 m, which was also the characteristic length derived from the autocorrelation function. The decay from the maximum of the pdf to the larger lengths l_W is exponential.

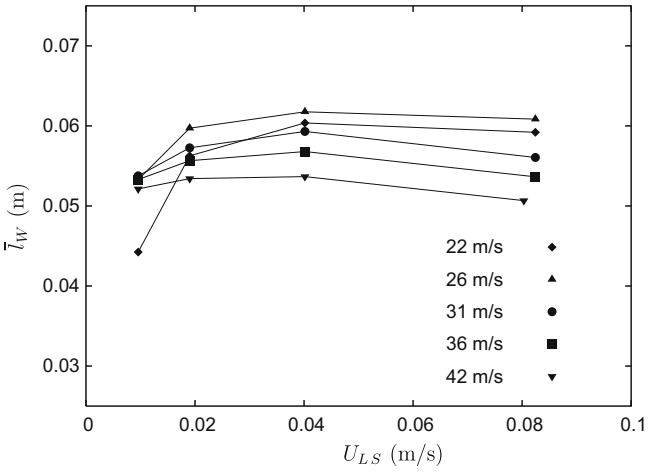

Fig. 29. Mean length of the disturbance waves $\bar{l}_W$ as a function of the liquid superficial velocities U_{LS}, for the different gas superficial velocities U_{GS}.

However, we are not sure whether this is physically-based. For instance, in a small number of cases, the local minima next to the disturbance wave do not go below the mean film thickness $\bar{\delta}$, although clearly they are in the base film. In that case, the length of the disturbance wave is overpredicted using the definition given above. However, the frequency at which this occurs is small and influences only the tails. Therefore, only the tails of the pdf in Figs. 30 and 31 should be handled with some caution.

5.6. Circumferential behavior of the disturbance waves

From the time-signals in Section 3 (see Fig. 9), it is clear that the height of each disturbance wave has large fluctuations in both the circumferential and axial direction. To quantify the three-dimensional structure of the disturbance waves, we measure for each disturbance wave the axial distance between the two maximum heights at two different circumferential positions (a reference circumferential position θ_{ref} and a second distinct circumferential position θ). The pdf of this axial separation distance is shown in Fig. 32, for different circumferential positions θ with respect to the reference position. Fig. 32 shows that the pdf are normally distributed around a zero separation distance. This means that, on average, the peaks are aligned perpendicu-

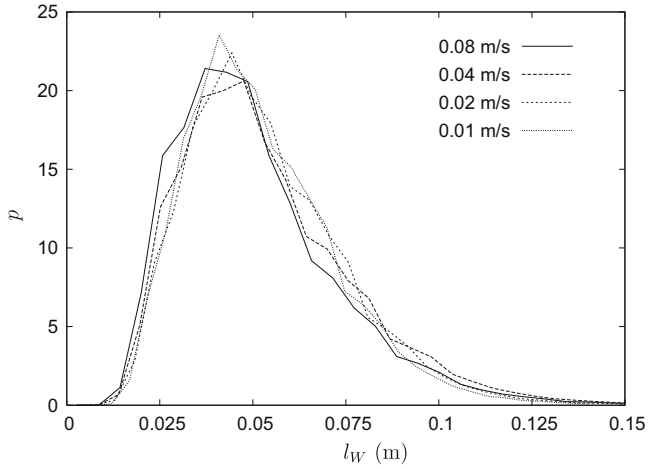

Fig. 30. Probability density function p of the wave length l_W, for different liquid superficial velocities U_{LS} at the highest gas superficial velocity U_{GS} = 42 m/s.

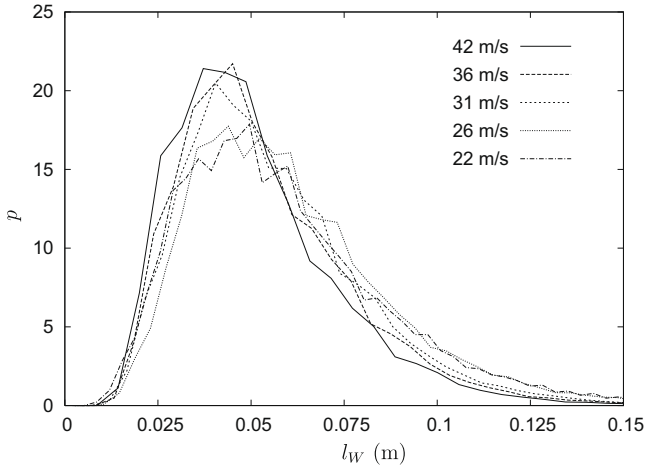

Fig. 31. Probability density function p of the wave length l_W, for different gas superficial velocities U_{GS} at the highest liquid superficial velocity U_{LS} = 0.08 m/s.

larly to the flow direction. This is also expected due to symmetry. However, the pdf are broadly distributed. The pdf at $\theta - \theta_{ref} = \pi/4$ shows that, already at a small angle, the peaks can be quite far apart, i.e. over the entire length of the disturbance wave. Therefore, the disturbance waves should be seen as a three-dimensional structure, with a meandering path between the peaks around the circumference.

Although the amount of disturbances waves is limited in the calculation of the pdf, Fig. 32 also seems to show that the spreading of the pdf becomes slightly larger for a circumferential position θ further from the reference position θ_{ref}. Furthermore, the probability of having an axial separation distance equal to 0.04 m between the peaks at two circumferential positions is not negligible. This distance should be compared to the mean length of the disturbance waves, roughly equal to 0.05 m. Therefore, the pdf in Fig. 32 indicates that the individual disturbance waves can flow with a slight inclination with respect to the mean flow direction. Indeed, Fig. 33, which consists of six consecutive snapshots of the film thickness, also suggests that the disturbance waves can flow with a slight inclination angle with respect to the axial direction.

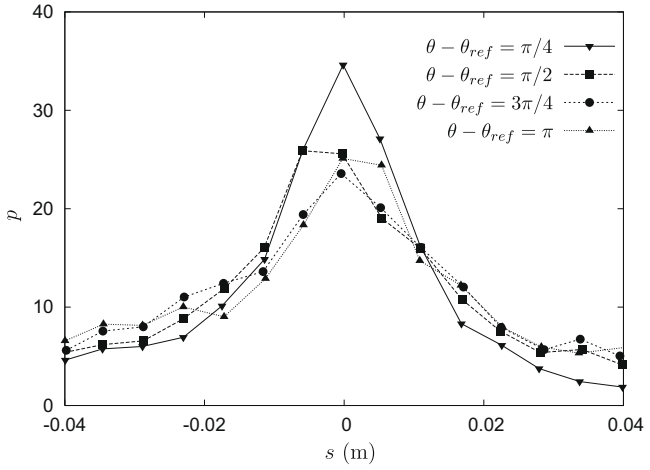

Fig. 32. Probability density function p of the axial distance s separating the maxima at two distinct circumferential positions θ_{ref} and θ in each disturbance wave. The gas and liquid superficial velocities are equal to U_{GS} = 42 m/s and U_{LS} = 0.08 m/s, respectively.

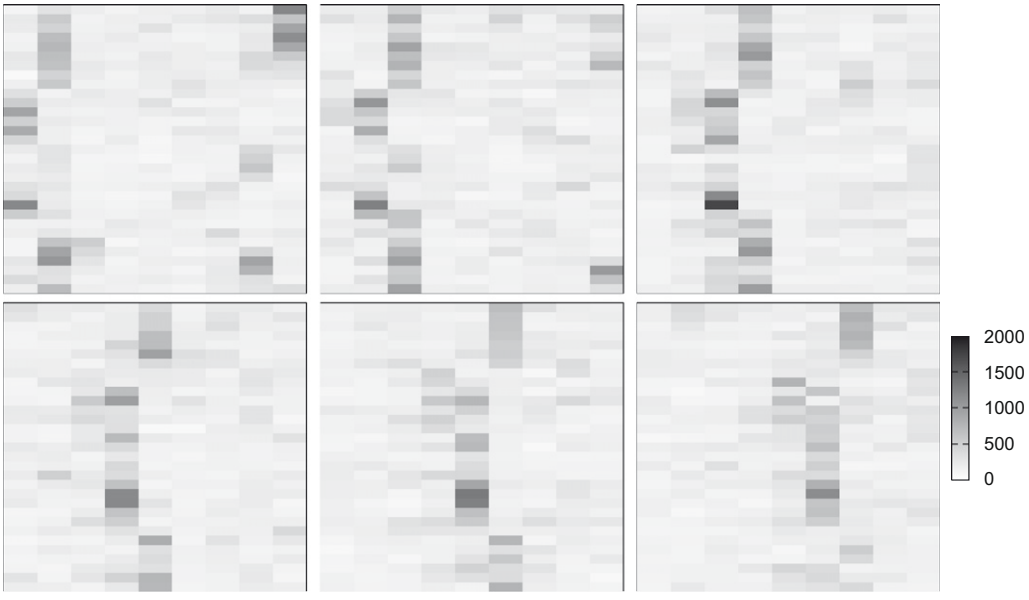

Fig. 33. From left to right, six consecutive contours of the raw instantaneous film thickness (in μm), which are separated by the time needed for a disturbance wave to travel from one axial location to the next, and is equal to roughly 0.006 s. The pipe is opened up for visualization purposes, i.e. the top and the bottom in the contours are in contact. U_{LS} = 0.02 m/s and U_{GS} = 42 m/s.

Note that the time cross-correlation between different receivers in the circumferential direction is maximum at about zero time-lag, which verifies that the disturbance waves are on average aligned perpendicularly to the flow direction. Note also that the disturbance waves are visually coherent over the length of the pipe, which indicates that this inclination does not have an effect on the coherence of the disturbance waves.

6. Conclusion

This work aims to provide a description of the interfacial structures in co-current vertical annular flow, with a special attention to the disturbance waves. To this end, a sensor has been developed to measure the film thickness with time and spatial resolution. The measurement technique is a non-intrusive conductivity-based technique, in which the film thickness is measured at 32 positions around the circumference times 10 positions in the axial direction, giving in total 320 measurement locations. Since the film thickness is measured at each measurement location between a pair of electrodes over a distance of 0.006 m, interfacial structures with a length smaller than roughly 0.006 m cannot be measured. Therefore, capillary ripples waves cannot be distinguished. However, we could identify two types of interfacial structures in co-current vertical annular flow: (i) large disturbance waves, and (ii) non-coherent height fluctuations. The main conclusions regarding both interfacial structures, obtained from measurements in an air/water vertical annular flow in a pipe of 0.05 m diameter, are given below.

The disturbance waves are shown to be truly three-dimensional structures. The height of each disturbance wave has large fluctuations in the circumferential direction as well as in the axial direction, with a meandering path between the maximum heights around the circumference. It also appears that the disturbance waves can flow with a slight inclination with respect to the circumferential direction. Further quantitative information on the height, length, velocity, frequency and spatial distribution has been given in terms of means and probability density functions. It appears that the mean length of the disturbance waves is roughly equal to the pipe diameter, and independent of the gas and liquid superficial velocities. Finally, the disturbance waves are shown to be located randomly in space, according to a Gamma distribution whose order only depends on the liquid superficial velocity. By the nature of the Gamma distribution, this could indicate that the spatial distribution of the disturbance waves results from a cascade of coalescence processes between the original disturbance waves on the film.

In between the disturbance waves, many non-coherent height fluctuations can be observed. Those height fluctuations were not the primary goal of this study, therefore they are described only qualitatively. It is shown that the non-coherent height fluctuations are also three-dimensional structures, with an amplitude smaller than that of the disturbance waves. Sometimes, however, they can become quite large, of the same order of the disturbance waves. This led Sekogushi and Takeishi (1989) and Wolf et al. (1996) to make a distinction between the smaller non-coherent height fluctuations and the larger ones, which they named "ephemeral" waves. However, based on the present observations, we do not see a fundamental difference between the small and large non-coherent height fluctuations. The length of the non-coherent height fluctuations varies, but globally their axial length is larger than roughly 0.01 m. Therefore, those structures, if they are waves, are probably not dominated by surface tension forces, i.e. they are not capillary ripple waves. Finally, we note that the part of the film thickness spectrum related to the non-coherent height fluctuations is similar to that for wind-generated gravity waves on oceans. This analogy could suggest that the existing theory on gravity waves on oceans might be used to characterize the non-coherent height fluctuations.

References

Asali, J.C., Hanratty, T.J., 1993. Ripples generated on a liquid film at high gas velocities. Int. J. Multiphase Flow 19 (2), 229–243.

Azzopardi, B.J., 1986. Disturbance wave frequencies, velocities and spacing in vertical annular two-phase flow. Nucl. Eng. Des. 92, 121–133.

Azzopardi, B.J., 1997. Drops in annular two-phase flow. Int. J. Multiphase Flow 23 (Suppl.), 1–53.

Badie, S., Lawrence, C.J., Hewitt, G.F., 2001. Axial viewing studies of horizontal gas–liquid flows with low liquid loading. Int. J. Multiphase Flow 27, 1259–1269.

Belt, R.J., 2007. On the liquid film in inclined annular flow. Ph.D. Thesis, Delft University of Technology.

Belt, R.J., Van't Westende, J.M.C., Portela, L.M., 2009. Prediction of the interfacial shear-stress in vertical annular flow. Int. J. Multiphase Flow 35, 689–697.

Brown, R.C., Andreussi, P., Zanelli, S., 1978. The use of wire probes for the measurement of liquid film thickness in annular gas–liquid flows. Can. J. Chem. Eng. 56, 754–757.

Chu, K.J., Dukler, A.E., 1975. Statistical characteristics of thin, wavy films. 3. Structure of the large waves and their resistance to gas flow. AIChE J. 21 (3), 583–593.

Coney, M.W.E., 1973. The theory and application of conductance probes for the measurement of liquid film thickness in two-phase flow. J. Phys. E: Sci. Instr. 6, 903–910.

Feller, W., 1971. An introduction to probability theory and its applications, second ed. Wiley and Sons, New York.

Fore, L.B., Dukler, A.E., 1995. Droplet deposition and momentum transfer in annular flow. AIChE J. 41 (9), 2040–2046.

Hanratty, T.J., 1991. Separated flow modelling and interfacial transport phenomena. In: Oliemans, R.V.A. (Ed.), Computational fluid dynamics for the petrochemical process industry. Appl. Sci. Res. 48, pp. 353–390.

Hewitt, G.F., Jayanti, S., Hope, C.B., 1990. Structure of thin liquid films in gas–liquid horizontal flow. Int. J. Multiphase Flow 16 (6), 951–957.

James, P.W., Wilkes, N.S., Conkie, W., Burns, A., 1987. Developments in the modelling of horizontal annular two-phase flow. Int. J. Multiphase Flow 13 (2), 173–198.

Jayanti, S., Hewitt, G.F., White, S.P., 1990. Time-dependent behaviour of the liquid film in horizontal annular flow. Int. J. Multiphase Flow 16 (6), 1097–1116.

Lopes, J.C.B., Dukler, A.E., 1986. Droplet entrainment in vertical annular flow and its contribution to momentum transfer. AIChE J. 32 (9), 1500–1515.

Marmottant, P., Villermaux, E., 2004. On spray formation. J. Fluid Mech. 498, 73–111.

Pan, L., Hanratty, T.J., 2002. Correlation of entrainment for annular flow in vertical pipes. Int. J. Multiphase Flow 28, 363–384.

Paras, S.V., Karabelas, A.J., 1991. Properties of the liquid layer in horizontal annular flow. Int. J. Multiphase Flow 17 (4), 439–454.

Phillips, O.M., 1985. Spectral and statistical properties of the equilibrium range in wind-generated gravity waves. J. Fluid Mech. 156, 505–531.

Prasser, H.-M., Boettger, A., Zschau, J., 1998. A new electrode-mesh tomograph for gas–liquid flows. Flow Measure. Instrum. 9, 111–119.

Prasser, H.-M., Zschau, J., Peters, D., Pietzsch, G., Taubert, W., Trepte, M., 2002. Fast wire-mesh sensors for gas–liquid flows – visualisation with up to 10000 frames per second. ICAPP 2002, Hollywood, FL. Paper 1055.

Schlichting, H., 1979. Boundary-Layer Theory, seventh ed. McGraw-Hill, New York.

Sekogushi, K., Takeishi, M., 1989. Interfacial structures in upward huge wave flow and annular flow regimes. Int. J. Multiphase Flow 15 (3), 295–305.

Van Maanen, H.R.E., 1999. Retrieval of turbulence and turbulence properties from randomly sampled laser-Doppler anemometry data with noise. Ph.D. Thesis, Delft University of Technology.

Van't Westende, J.M.C., Kemp, H.K., Belt, R.J., Portela, L.M., Mudde, R.F., Oliemans, R.V.A., 2007. On the role of droplets in cocurrent annular and churn-annular pipe flow. Int. J. Multiphase Flow 33 (6), 595–615.

Wallis, G.B., 1969. One Dimensional Two-Phase Flow. McGraw-Hill, New York.

Wolf, A., Jayanti, S., Hewitt, G.F., 1996. On the nature of ephemeral waves in vertical annular flow. Int. J. Multiphase Flow 22 (2), 325–333.

Woodmansee, D.E., Hanratty, T.J., 1969. Mechanism for the removal of droplets from a liquid surface by a parallel air flow. Chem. Eng. Sci. 24, 299–307.

Zabaras, G., Dukler, A.E., Moalem-Maron, D., 1986. Vertical upward cocurrent gas–liquid annular flow. AIChE J. 32 (5), 829–843.